Energy dissipation in violent three dimensional sloshing flows induced by high-frequency vertical accelerations

J. Michel,[1, a)] D. Durante*,[1, b)] A. Colagrossi,[1, 2, c)] and S. Marrone[1, d)]

[1)] *CNR-INM, Institute of Marine Engineering, 00128, Rome, Italy*

[2)] *ECN / CNRS, École Centrale Nantes, LHEEA Lab., 44300, Nantes, France*

The European H2020 project SLOWD is aimed at investigating the fuel sloshing damping effect to reduce the design loads on aircraft wings. Wings house the fuel tanks and are highly flexible structures that can significantly deform under gust loads. In the recent experiment by Martinez-Carrascal and González-Gutiérrez [J. Fluids and Structures **100**, 103172 (2021)] the complex problem of the fuel sloshing inside a flexible wing structure was significantly simplified by considering a partially filled vertically heaving tank attached to a system of springs. In the present research a Smoothed Particle Hydrodynamic model was adopted to evaluate the energy dissipated in the three-dimensional sloshing flow obtained using the same tank motions. From a numerical point of view the simulation of such a violent flow is rather challenging, the involved vertical accelerations being as large as $10g$. The resulting flow is extremely complex because of the severe turbulence developed, the violent impacts and the considerable fragmentation of the air-liquid interface. The role of the viscosity is investigated by taking into account two different liquids. Finally, some comparisons between three-dimensional results and previous two-dimensional studies are also discussed.

PACS numbers: 47.11.-j, 47.15.-x, 47.10.ad

Keywords: Smoothed Particle Hydrodynamics, Sloshing Flows, Large Eddy Simulations

[a)]Electronic mail: julien.michel@inm.cnr.it

[b)]Electronic mail: danilo.durante@cnr.it (corresponding author)

[c)]Electronic mail: andrea.colagrossi@cnr.it

[d)]Electronic mail: salvatore.marrone@cnr.it

I. INTRODUCTION

Sloshing flows are those occurring when free surface waves are generated inside a tank. They are caused by any disturbance to partially filled liquid containers. As clarified in Ibrahim [1], depending on the type of disturbance and container shape, the liquid surface can experience different types of motion including simple planar, rotational, symmetric, asymmetric, quasi-periodic or chaotic. The interaction with the container walls may induce significant global and local loads because of the impacts of the travelling waves. The basic problem of liquid sloshing involves the estimation of the hydrodynamic pressure distribution, forces, moments and natural frequencies of the free surface oscillation. The sloshing motion is characterised by an infinite number of natural frequencies, but only the few lowest modes are the most likely to be excited by the tank motion. Moreover, the nonlinear effects associated with the free-surface motion are different from nonlinear water waves in ocean and rivers, presenting amplitude jumps, parametric resonance, chaotic motion and nonlinear sloshing mode interaction (Ibrahim [1], Faltinsen and Timokha [2]). These sloshing modes may directly affect the stability and performances of moving containers. Because of this, a large number of studies have been recently dedicated to the damping/suppression of unwanted oscillations.

On the other hand, sloshing flows can be effectively used to dampen the oscillations of a structure. Tuned Liquid Dampers (TLD) exploit the liquid sloshing motion in a tank in order to counteract the external forces and dissipate energy. These dampers are of great interest in many engineering fields, spanning from the control of building stability (Tamura *et al.* [3], Novo *et al.* [4], Kareem *et al.* [5], Yamamoto and Sone [6]) or the rolling motion of ships (Bass [7]) in the civil engineering, to aerospace where the suppression of spacecraft instabilities is of fundamental importance during the ascent or landing stages (Graham and Rodriguez [8], Abramson [9]).

From the physical point of view, the study of the dissipation induced by a free-surface flow is arduous, especially in the presence of wave breaking. Cooker [10,11] performed decay experiments with a free oscillating tank, suggesting that hydraulic jump theory can provide some insight into the dissipation mechanisms. Perlin *et al.* [12] presented a review of studies dedicated to the dissipation caused by wave breaking. From a numerical point of view, potential flow theory (Frandsen [13]) as well as shallow water approximation (Ardakani and Bridges [14], Ardakani *et al.* [15]) have been adopted for the simulation of sloshing flows and

the study of energy dissipation. In his pioneering works Demirbilek[16,17,18] investigated the dissipation in sloshing waves both theoretically and numerically, by considering a linearized stream function formulation of 2D momentum equations. Some results of the influence of both Froude and Reynolds numbers on the dissipation values were deduced but no validation was provided. More recently, Reed *et al.*[19] investigated experimentally and numerically the effects of large amplitude sloshing on a TLD, while Marsh *et al.*[20] performed a numerical study regarding the analysis of damping properties of egg-shaped sloshing tanks. In Bouscasse *et al.*[21] and Bouscasse *et al.*[22] a dynamical system involving a driven pendulum filled with liquid was studied experimentally and numerically by Smoothed Particle Hydrodynamics (SPH), focusing on the mechanical energy dissipation of the system.

A recent and attractive example of an industrial sloshing problem, that has increasingly received attention, concerns the kerosene containers placed inside aircraft wings subjected to external wind gusts. Although typical attitude corrections cause weak fuel sloshing motions because of the low accelerations involved, sudden strong gusts accelerate the fuel transversely up to values of 10g, which results in amplitudes comparable to the tank dimensions and frequencies higher than 5 Hz (see Gambioli and Malan[23]). This fluid motion, which several experiments have demonstrated to play a role on the damping of the wing vibrations, is significantly different from typical sloshing flows: the fuel is continuously broken into several jets and drops, whilst violently slamming alternately upward and downward against the tank walls.

Disregarding their industrial impact, very few studies dealing with vertically sloshing flows are found in the literature. Experimentally, one of the first studies dealing with this problem was Bredmose *et al.*[24] and, more recently, Gambioli and Malan[25]. Titurus *et al.*[26] carried out an experimental campaign devoted to reproducing the same conditions as those found for aircraft wing tanks, at model scale. In those experiments, a partially filled tank was bounded to an elastic beam, which was deformed and released in such a way that the tank moved with a heaving oscillatory motion, where accelerations up to 10g could be reached. Constantin *et al.*[27,28] discussed a combination of experiments and analytical studies, where the sloshing-induced energy dissipation was investigated with a controlled vertically oscillating and partially filled fluid container. The authors also suggested a particle ballistic model to further explain the nature of the damping saturation point. In Martinez-Carrascal and González-Gutiérrez[29] a one-degree-of-freedom experimental campaign on a

partially filled heaving tank attached to a system of springs was carried out. In that case the damping action of the sloshing flow on the tank oscillations was studied in detail, by taking into account several non-dimensional parameters.

Ongoing European projects, such as the EU-SLOWD (Gambioli *et al.*[30]) are planning ambitious experimental campaigns in the future that include a full scale aircraft wing structure with the corresponding fuel tanks. This structure will be excited to the most critical conditions for which sloshing effects are likely to be relevant.

From the numerical point of view, violent internal flows are challenging to simulate and mesh-based numerical approaches may suffer from significant mass loss if *ad-hoc* strategies are not adopted (see *e.g.* Broglia and Durante[31]). Conversely, particle based approaches such as SPH are more suitable for these kinds of simulations where the free surface is strongly and rapidly deformed in jets and fragmented in sprays and drops.

In Marrone *et al.*[32], the initial stages of such violent flows, where the liquid is mainly driven by inertia because of the strong accelerations, are referred to as "shaken flow". Later stages of the problem, where most of the energy has been dissipated and the tank accelerations become smaller than gravity, are classified as "sloshing flows". In Marrone *et al.*[32], the δ-LES-SPH method was used to study the energy dissipation mechanisms, occurring in shaken flows, for tanks subjected to vertical oscillatory motions with accelerations as high as $10g$. In a second paper by Marrone *et al.*[33] the experiments of Martinez-Carrascal and González-Gutiérrez[29] were used as reference for comparisons with the numerical simulations.

In the present paper the same experimental campaign of Martinez-Carrascal and González-Gutiérrez[29] is taken into account and, similarly to Marrone *et al.*[32], the δ-LES-SPH approach is adopted for the simulation of the liquid phase only, neglecting the air phase. Unlike the work of Marrone *et al.*[32] and Marrone *et al.*[33], where the analysis was entirely carried out under the 2D assumption, here the analysis is fully 3D, thus implying additional complications in accurately resolving the flow field, as will be stressed in the following.

One of the typical drawbacks of the standard SPH method is the so-called "tensile instability" which develops inside the fluid domain inducing numerical cavitations in low pressure regions. Conversely, in the δ-LES-SPH model adopted in the present work, a particle shifting technique (PST) enforcing uniform distributions, discussed in Sun *et al.*[34], is adopted to avoid the development of tensile-instability. Furthermore, the use of PST largely

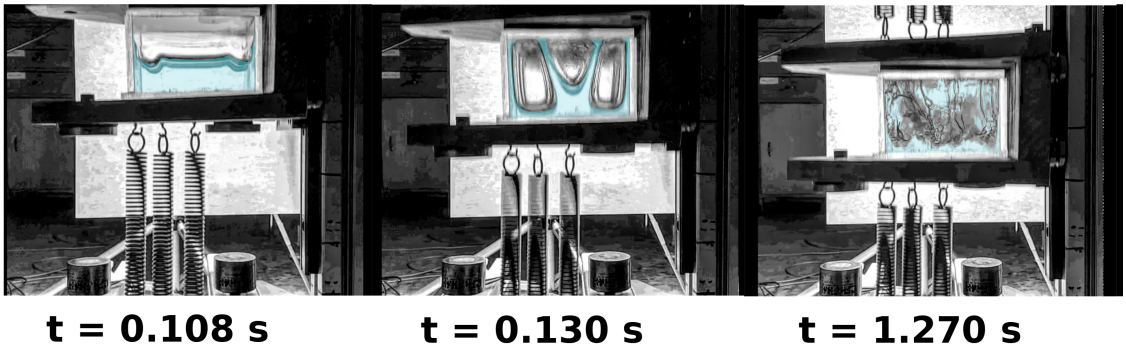

Figure 1. Experimental snapshots of the SDOF vertical sloshing water experiments carried out in Martinez-Carrascal and González-Gutiérrez [29] for 50% filling level.

.

improves the accuracy of the integral interpolations allowing a more accurate evaluation of pressure and vorticity fields. Finally, a Large Eddy Simulation (LES) approach based on the classical Smagorinsky model is included in the numerical scheme (see Di Mascio *et al.* [35], Antuono *et al.* [36] for details) so that the energy contributions coming from unresolved turbulent scales are taken into account.

The paper is organized as follows: in section II the experimental conditions are outlined; in section III the governing equations are introduced; in section IV the numerical scheme is discussed; in section V some considerations on the energy dissipation are presented; in section VI the simulations with oil and water are discussed and the results compared with the 2D outcomes. Furthermore, a deep insight into energy dissipation is offered in section VI B. Finally, conclusions are given in section VII.

II. PROBLEM DESCRIPTION

In the present numerical study the conditions adopted in the experimental campaign by Martinez-Carrascal and González-Gutiérrez [29] are applied. In that work a violent sloshing flow in a vertically moving tank was experimentally studied. A tank measuring $10\times6\times6$ cm is connected to a set of 6 springs, 3 on the upper side and 3 on the lower side, as sketched in figure 1.

In the present work, water and oil are considered as sloshing liquids. The tank is filled up to 50% of its volume (water mass of $m_l = 0.18$ kg and oil $m_l = 0.162$ kg).

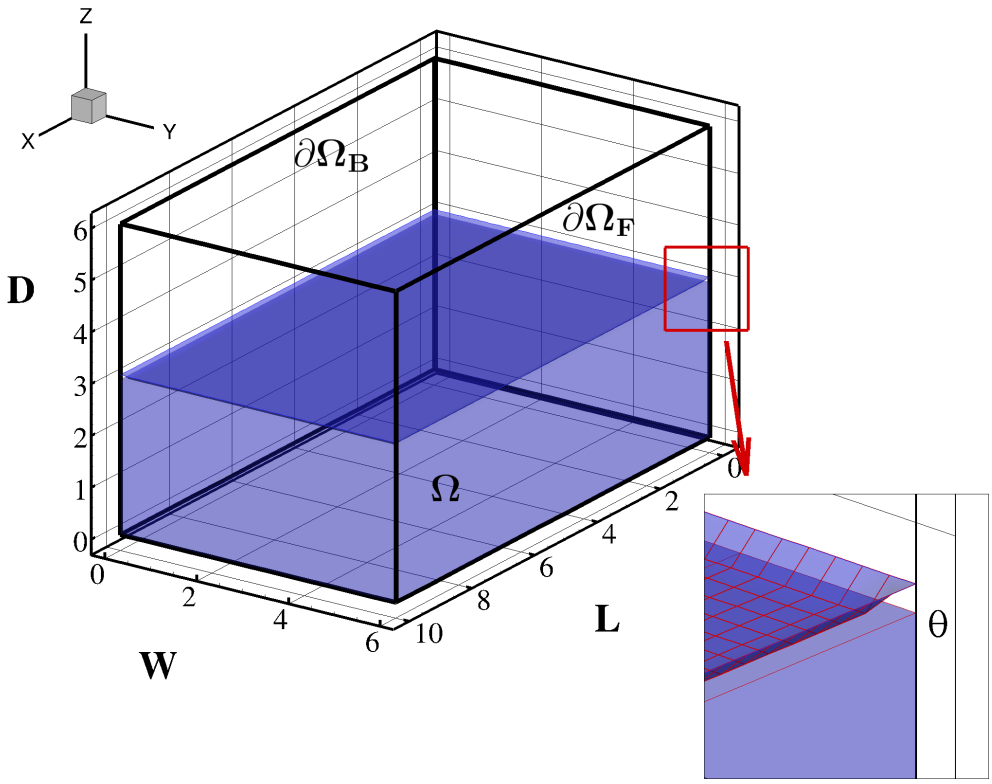

Figure 2. Experimental box sketch with highlight of the filled volume. The axes scales are in cm. Bottom-right: an enlarged view of the liquid meniscus.

When the springs are released, for both the liquids, the tank oscillates at a characteristic frequency of about $f_0 = 1/T = 6.51$ Hz. At time $t = T$ the tank reaches its maximum vertical displacement $2A = 1.14L$ and a maximum deceleration about $-9.3g$. The maximum velocity $U_{\max}$ of about 2.33 m/s is reached by the tank at $t = 0.747T$ during the first rising stage, while the maximum acceleration a_{max} of about More details on the experiment can be found in the article by Martinez-Carrascal and González-Gutiérrez [29].

The problem geometry considered in the present work is sketched in figure 2, where L = 10 cm, D = 6 cm, W = 6 cm and H = 3 cm. In the same plot the liquid menisci due to the contact angle between the lateral walls and the liquid surface are depicted and enlarged in the inset. The Reynolds number of the problem is referred to the maximum tank velocity (Re $= U_{max}L/\nu$) where ν is the kinematic viscosity of the fluid.

The tank motions are imposed and are only in the vertical direction. The law of motion is taken from acceleration measurements in Martinez-Carrascal and González-Gutiérrez [29] and the motion follows a decay law. The kinematic viscosity, ν, for the water and oil are,

respectively, $10^{-6}\,m^2/s$ and $5\times10^{-5}\,m^2/s$. The resulting Reynolds numbers for water and oil using the above quantities are equal to 233,000 and 4660.

III. GOVERNING EQUATIONS

In the present work a three-dimensional fluid domain $\boldsymbol{\Omega}$ is considered with its boundaries which are composed by the tank walls $\partial\boldsymbol{\Omega}_B$ and the free surface $\partial\boldsymbol{\Omega}_F$. The flow evolution is governed by the Navier-Stokes equations (see also Marrone *et al.*[32,33]):

$$\begin{cases} \dfrac{D\rho}{Dt} = -\rho\,\mathrm{div}(\boldsymbol{u}), & \dfrac{D\boldsymbol{u}}{Dt} = \boldsymbol{g} + \dfrac{\mathrm{div}(\mathbb{T})}{\rho} \\ \dfrac{De}{Dt} = \dfrac{\mathbb{T}:\mathbb{D}}{\rho}, & \dfrac{D\boldsymbol{r}}{Dt} = \boldsymbol{u}, \qquad p = f(\rho) \end{cases} \tag{1}$$

with D/Dt the Lagrangian derivative, $\boldsymbol{r}$ the material points positions, $\boldsymbol{u}$ the flow velocity, ρ the fluid density, e the specific internal energy, $\mathbb{T}$ the stress tensor, $\mathbb{D}$ the rate of strain tensor and $\boldsymbol{g}$ the gravitational acceleration.

The liquid is assumed to be Newtonian and the flow isothermal, while the surface tension effects are neglected, *i.e*: $\mathbb{T} = [-p + \lambda\,\mathrm{div}(\boldsymbol{u})]\,\mathbb{I} + 2\,\mu\,\mathbb{D}$, where μ and λ are the primary and secondary dynamic viscosity of the liquid and $\mathbb{I}$ is the identity tensor.

The eq. (1) can be solved either in an Inertial Frame of Reference (I-FoR) where the tank is moving or in a Non-inertial Frame of Reference (Ni-FoR) which moves with the tank. If the fluid motion is considered within the Ni-FoR, the non-inertial accelerations $\boldsymbol{f}_{NI}$ due to the tank motion must be taken into account in the governing equations 1:

$$\begin{cases} \dfrac{D\rho}{Dt} = -\rho\,\mathrm{div}(\hat{\boldsymbol{u}}), & \dfrac{D\hat{\boldsymbol{u}}}{Dt} = \hat{\boldsymbol{g}} + \boldsymbol{f}_{NI} + \dfrac{\mathrm{div}(\hat{\mathbb{T}})}{\rho} \\ \dfrac{De}{Dt} = \dfrac{\hat{\mathbb{T}}:\hat{\mathbb{D}}}{\rho}, & \dfrac{D\hat{\boldsymbol{r}}}{Dt} = \hat{\boldsymbol{u}}, \qquad p = f(\rho) \end{cases} \tag{2}$$

where the hat symbol $\hat{}$ is used for the quantities described in the Ni-FoR.

Although the description of the phenomena in both frames of reference does not affect the evaluation of the energy dissipated during the liquid motions, different numerical approaches may lead to different numerical errors, depending on this choice. In order to avoid numerical errors due to the tank motion, in the present work the Ni-FoR is considered.

By considering that the temperature is assumed to be constant since the effects of its variation are negligible with a good approximation, as we underlined above, the pressure p is

assumed to depend on the density only. Furthermore, since a weakly-compressible condition is assumed, a simple linear equation of state can be adopted:

$$p = c_0^2 \, (\rho - \rho_0) \tag{3}$$

where c_0 plays the role of a constant speed of sound of the liquid and ρ_0 is the density at the free-surface (where p is assumed to be equal to zero).

The weakly-compressible hypothesis implies the following requirement:

$$c_0 \gg \max\left(U_{max}, \sqrt{\frac{(\Delta p)_{max}}{\rho_0}}\right) \tag{4}$$

where U_{max} and $(\Delta p)_{max}$ respectively are the maximum fluid speed and the maximum pressure variation expected (with respect to the zero pressure free-surface level) in $\mathbf{\Omega}$. By considering that the time integration is performed with a time step related to the value of c_0, the latter is always set lower than its physical counterpart (in the present work, about two orders of magnitude lower). The constraint (4), however, must be checked in order to guarantee the weakly-compressible regime.

The simplifications adopted for the physical model are, in summary:

- the air phase is not considered;
- thermal conductivity and surface tension are neglected;
- a weakly-compressible condition is obtained with an artificial speed of sound.

Neglecting the gas phase may appear inappropriate for violent sloshing simulations where the air entrapment is unavoidable. For instance, Lamarre and Melville[37] estimated that the work done against buoyancy in entraining air accounted for up to 50%. However, in the present case the rapid succession of impacts against, alternatively, the ceiling and the floor of the tank makes the flow rather different from a breaking wave. Further, in Marrone *et al.*[38], it was shown that, although the air phase plays a relevant role in the flow evolution, the evaluation of the energy dissipation in violent flows even under the single-phase hypothesis is still accurate enough. A further confirmation can also be found in Bouscasse *et al.*[21,22] where the study of the mechanical energy dissipation induced by sloshing and wave breaking in a fully coupled angular motion system was investigated. In that work it was shown that a single-phase SPH model is able to correctly predict the experimental fluid dissipated

energy. Another confirmation is given in[39] for the application to spillway hydraulics where an extensive comparison is made between the single-phase and two-phase water–air modelling approaches.

As far as surface tension effects are concerned, these are relevant above all during the initial stage. As remarked in Marrone *et al.*[32,33], during the initial intense vertical acceleration, a Rayleigh–Taylor instability develops. The latter is triggered by the fluid meniscus formed at the intersection between the lateral walls and the liquid surface and numerically modelled as indicated in figure 2. In the evolution just afterwards, the role of the surface tension becomes negligible according to the velocity and length scales considered, as also explained in Calderon-Sanchez *et al.*[40], since the Weber number, $\mathrm{We} = \rho\, U_{max}^2\, L/\sigma$ (where σ is the surface tension coefficient of the liquid considered) is larger than 4,000 for both the liquids considered in this work. Therefore, the surface tension force terms are neglected while initial effect of surface tension is recovered by appropriately setting the initial meniscus free-surface deformation with an angle $\theta = 45°$ (see inset of figure 2).

Finally, as clarified in Marrone *et al.*[41] and in Meringolo *et al.*[42], the energy dissipation related to the water impacts as predicted by using the artificial speed of sound within the weakly-compressible assumption (see equation (1)) is consistent with the one predicted by incompressible flow models.

A. Subgrid models

As reported in section II the water test-case is characterised by a Reynolds number equal to 233,000. Therefore, in the numerical scheme a subgrid model for the turbulent viscosity is needed. For the choice of the sub-grid models the articles by Christensen and Deigaard[43,44] are considered. In those works a simple LES with Smagorinsky model is adopted for simulating breaking waves. The same LES model was adapted in the SPH framework by Di Mascio *et al.*[35] and further enhanced in Antuono *et al.*[36] by introducing LES modelling in a quasi-Lagrangian formalism. The latter formulation is one adopted also in the present work. More complex models, such as the dynamic LES model adopted in Lubin and Glockner[45], can be also considered for future works but they should be preliminary adapted and validated in the SPH framework. As remarked in Labourasse *et al.*[46] it is worth noting that turbulence models in violent free-surface and multiphase flows still remain an

open problem nowadays.

IV. NUMERICAL SCHEME

The δ-LES-SPH model presented in Antuono *et al.*[36], Meringolo *et al.*[47] is here briefly recalled and the interested reader is addressed to the detailed discussions therein. The governing equations (1) are discretized according to the Smoothed Particle Hydrodynamics numerical approach:

$$\begin{cases} \dfrac{\mathrm{d}\rho_i}{\mathrm{d}t} &= \displaystyle\sum_j \left[-\rho_i\ (\boldsymbol{u}_{ji} + \delta\boldsymbol{u}_{ji}) + (\rho_j\ \delta\boldsymbol{u}_j + \rho_i\ \delta\boldsymbol{u}_i)\right] \cdot \nabla_i W_{ij} V_j + \mathcal{D}_i^{\rho} \\ \rho_i \dfrac{\mathrm{d}\boldsymbol{u}_i}{\mathrm{d}t} &= \displaystyle\sum_j \left[-(p_j + p_i)\ \mathbb{I} + \rho_0(\boldsymbol{u}_j \otimes \delta\boldsymbol{u}_j + \boldsymbol{u}_i \otimes \delta\boldsymbol{u}_i)\right] \cdot \nabla_i W_{ij} V_j + \boldsymbol{F}_i^{v} + \rho_i \boldsymbol{g} \\ \dfrac{\mathrm{d}\boldsymbol{r}_i}{\mathrm{d}t} &= \boldsymbol{u}_i + \delta\boldsymbol{u}_i, \quad V_i(t) = m_i \,/\, \rho_i(t), \quad p = c_0^2(\rho - \rho_0) \end{cases} \tag{5}$$

where the index i refers to the considered particle and j refers to neighbour particles of i. The vector $\boldsymbol{F}_i^v$ is the net viscous force acting on the particle i, while $\delta\boldsymbol{u}$ is the Particle Shifting velocity field which acts on the spatial distribution of the particles during their motion, rearranging them in a more regular configuration. The mass m_i of the $i-$th particle is assumed to be constant during its motion. The particles are set initially on a Cartesian lattice with spacing Δr, and hence, the volumes V_i are initially set as Δr^3. The particle masses m_i are calculated through the initial density field (using the equation of state and the initial pressure field) and remain constant during the time evolution. The volumes V_i change in time accordingly with the particle density (see bottom line of eq. (5)). The spatial gradients are approximated through the convolution with a kernel function W_{ij}. Following Antuono *et al.*[36], a C2-Wendland kernel is adopted in the present work.

The time derivative d/dt used in (5) indicates a quasi-Lagrangian derivative, *i.e.*:

$$\frac{d(\bullet)}{dt} := \frac{\partial(\bullet)}{\partial t} + \nabla(\bullet) \cdot (\boldsymbol{u} + \delta\boldsymbol{u})$$

since the particles are moving with the modified velocity $(\boldsymbol{u}+\delta\boldsymbol{u})$ and the first two equations of (5) are written following an Arbitrary Lagrangian-Eulerian approach. Because of this, the continuity and the momentum equations contain terms with spatial derivatives of $\delta\boldsymbol{u}$ (for details, the interested reader is referred to Antuono *et al.*[48]).

The notation $\boldsymbol{u}_{ji}$ in (5) indicates the differences $(\boldsymbol{u}_j - \boldsymbol{u}_i)$ and the same holds for $\delta\boldsymbol{u}_{ji}$ and $\boldsymbol{r}_{ji}$. The spurious noise in the pressure field is filtered out through the diffusive term $\mathcal{D}_i^{\rho}$,

introduced by Antuono *et al.*[49]. Following Antuono *et al.*[36], this term is included together with a LES model as follows:

$$\begin{cases} \mathcal{D}_i^{\rho} \;:=\; \displaystyle\sum_j \delta_{ij}\, \boldsymbol{\psi}_{ji} \cdot \nabla_i W_{ij}\, V_j \\ \boldsymbol{\psi}_{ji} \;:=\; 2\left[(\rho_j - \rho_i) - \dfrac{1}{2}\left(\langle\nabla\rho\rangle_i^L + \langle\nabla\rho\rangle_j^L\right)\cdot \boldsymbol{r}_{ji}\right] \dfrac{\boldsymbol{r}_{ji}}{||\boldsymbol{r}_{ji}||^2} \\ \delta_{ij} \;:=\; 2\,\dfrac{\nu_i^{\delta}\,\nu_j^{\delta}}{\nu_i^{\delta} + \nu_j^{\delta}} \qquad \nu_i^{\delta} := (C_{\delta}\, l)^2\, ||\mathbb{D}_i|| \end{cases} \tag{6}$$

where C_δ is a dimensionless constant (typically set to 6.0), while $l = 2.7\Delta r$ is the radius of the support of the kernel W for three spatial dimensions ($l = 4\Delta r$ in two dimensions, see Marrone *et al.*[32]) and represents the length scale of the filter adopted for the LES sub-grid model. $||\mathbb{D}||$ is a rescaled Frobenius norm, namely $||\mathbb{D}|| = \sqrt{2\mathbb{D} : \mathbb{D}}$. The superscript L in (6) indicates that the gradient is evaluated through the renormalized gradient equation, *i.e.*:

$$\langle\nabla\rho\rangle_i^L \;=\; \sum_j (\rho_j - \rho_i)\, \mathbb{L}_i^{-1}\, \nabla_i\, W_{ij}\, V_j\,, \qquad \mathbb{L}_i := \left[\sum_k (\boldsymbol{r}_k - \boldsymbol{r}_i) \;\otimes\; \nabla_i\, W_{ik}\, V_k\right] \tag{7}$$

where $\mathbb{L}_i$ is the renormalization matrix (see *e.g* Antuono *et al.*[50]).

The viscous forces $\boldsymbol{F}^v$ are expressed as:

$$\begin{cases} \boldsymbol{F}_i^v \;:=\; K \displaystyle\sum_j (\mu \;+\; \mu_{ij}^T)\, \pi_{ij}\, \nabla_i W_{ij}\, V_j \qquad\qquad K := 2(n+2) \\ \pi_{ij} \;:=\; \dfrac{\boldsymbol{u}_{ij}\cdot\boldsymbol{r}_{ij}}{||\boldsymbol{r}_{ji}||^2} \qquad \mu_{ij}^T \;:=\; 2\,\dfrac{\mu_i^T\,\mu_j^T}{\mu_i^T + \mu_j^T} \qquad \mu_i^T \;:=\; \rho_0\,(C_S\, l)^2\, ||\mathbb{D}_i|| \end{cases} \tag{8}$$

where n is the number of spatial dimensions and C_S is the so called Smagorinsky constant, set equal to 0.18 (see Smagorinsky[51] and Bailly and Comte-Bellot[52]). The viscous term (8) contains both the effect of the physical viscosity μ as well as of the one related to the turbulent stresses μ_i^T (see also the pioneering articles[53],[54]).

When considering violent free-surface flows, $||\mathbb{D}||$ can exhibit a singular behaviour in the limit $l \to 0$, especially during impacts, and can reach unlimited values; therefore, in order to avoid stability issues the terms μ_{ij}^T and δ_{ij} are limited with upper bounds equal to, respectively, $\mu_{ij}^T = 0.1\, l\, c_0\, \rho_0 / K$ and $\delta_{ij} = 0.1\, l\, c_0$.

Finally, consistently with[32], the Particle Shifting velocity $\delta \boldsymbol{u}$ is given by:

$$\begin{cases} \delta \boldsymbol{u}_i^* &= -U_{\max}\, l \sum_j \left[1 + R \left(\dfrac{W_{ij}}{W(\Delta r)} \right)^n \right] \nabla_i W_{ij} V_j \\ \delta \boldsymbol{u}_i &= \min \left(||\delta \boldsymbol{u}_i^*||, \dfrac{\max_j \, ||\boldsymbol{u}_{ij}||}{2}, \dfrac{U_{\max}}{2} \right) \dfrac{\delta \boldsymbol{u}_i^*}{\left\| \delta \boldsymbol{u}_i^* \right\|} \end{cases} \tag{9}$$

The constants R and n are respectively set to 0.2 and 4 as in Sun *et al.*[34], Monaghan[55]. The second equation of (9) is introduced to limit the magnitude of the shifting velocity for the sake of robustness. Since formulae (9) are proportional to the smoothing length, the finer the spatial resolution the lower the intensity of $\delta \boldsymbol{u}$, thus guaranteeing that $\delta \boldsymbol{u}_i$ induces small deviations on the physical particle trajectories. As documented in Sun *et al.*[34], the use of the Particle Shifting Technique (PST) leads to regular particle distributions and increases the accuracy and the robustness of the scheme. Further, as shown in Marrone *et al.*[32] the use of a PST is crucial in the considered problem where the occurrence of tensile instability is expected due to the development of intense negative pressure. As discussed in detail in Sun *et al.*[34] and Antuono *et al.*[48] the use of a PST alters the exact conservation of the angular momenta and may induce errors on the conservation of the total volume occupied by the fluid. The latter inconvenience is substantially limited by including the PST within an Arbitrary Lagrangian-Eulerian framework. We remark that total volume preservation is also influenced by time stepping and the adopted CFL conditions as discussed below.

It is worth noting that the shifting velocity close to the free surface has to be modified to be consistent with the kinematic boundary condition along such an interface. In particular, the normal component of $\delta \boldsymbol{u}$ to this interface has to be nullified while the tangential component is maintained unaltered (for more details, see Sun *et al.*[34]). In Khayyer *et al.*[56] it was shown that the choice of the PST in the free-surface region may also adversely affect the mechanical energy of the scheme. However, as also shown in Sun *et al.*[34] the PST adopted in the present work has only a minor influence on the mechanical energy (see also the recent work in Michel *et al.*[57]).

A 4th-order Runge-Kutta scheme is adopted to integrate in time system (5). The time step, Δt, is obtained as the minimum over the following bounds as set by Courant-Friedrichs-

Lewy conditions:

$$\begin{cases} \Delta t_v \;=\; 0.031 \min\limits_i \dfrac{l^2\,\rho_i}{(\mu+\mu_i^T)}\,, \quad \Delta t_a \;=\; 0.3 \min\limits_i \sqrt{\dfrac{\Delta r}{\|\boldsymbol{a}_i\|}}\,, \quad \Delta t_c \;=\; 0.6\left(\dfrac{l}{c_0}\right), \\ \\ \Delta t \;=\; \min(\Delta t_v\,, \Delta t_a\,, \Delta t_c) \end{cases} \tag{10}$$

where l is the radius of the kernel support, $\|\boldsymbol{a}_i\|$ is the particle acceleration, Δt_v is the time step related to viscosity, Δt_a is the advective time step and Δt_c is the acoustic time step (see *e.g.*[58]). For the problem addressed in this work the last two constraints are always the most restrictive. Specifically, the term Δt_a plays a relevant role when shifting velocity is large, *e.g.* during impacts. This contributes to a better preservation of the volume occupied by the fluid. The latter was checked at the end of the simulations where it was verified that the relative error on the total volume is maintained below 5%.

A. Boundary conditions

The governing equations (1) are coupled with kinematic and dynamic free-surface boundary conditions on $\partial\Omega_F$, while on the solid surfaces $\partial\Omega_B$ the no-slip boundary condition needs to be enforced. Concerning the former, free-surface boundary conditions are intrinsically satisfied in SPH methods (see Colagrossi *et al.*[59]). On the other hand, in SPH it is difficult to resolve thin wall boundary layers (WBL) unlike mesh-based methods. Indeed, the use of smaller particles close to the walls implies large CPU costs linked to the explicit time integration of the scheme, as the time steps decrease proportionally to the particle size. Consequently, if the fluid viscosity is significantly low (*i.e.* high Reynolds numbers) very thin WBLs are developed. Because they are too demanding in terms of computational resources to be well resolved, a simple no-penetration boundary condition (free-slip) is preferred.

In the present paper the Reynolds number of the simulations with water is about 233,000. From a rough estimation of the WBL thickness it turns out that, with the maximum spatial resolutions adopted, the near wall regions are still under-resolved so that free-slip conditions are preferred. Conversely, the simulations with oil are performed at a Reynolds number of about 4,660. The same particle size as for water is sufficient to resolve the boundary layer developed by the oil, thus allowing the no-slip conditions to be considered.

An evaluation of the limit of the free-slip assumption for the water simulations is given in Marrone *et al.*[32]. It was concluded that for the kind of violent free-surface flows studied in the present work, the energy dissipation is not substantially affected by the choice of the wall boundary conditions. This result is also linked to two opposing phenomena: the wall friction implies a further energy dissipation mechanism but, on the other hand, it slows down the run-up of the liquid jet, decreasing the intensity of the liquid impact against the tank walls.

V. CONSIDERATIONS ON THE ENERGY DISSIPATION

Following the analysis performed in Antuono *et al.*[60] and in Meringolo *et al.*[47] the δ-LES-SPH energy balance can be written as:

$$\dot{\mathcal{E}}_M + \dot{\mathcal{E}}_C = \mathcal{P}_V + \mathcal{P}_V^{turb} + \mathcal{P}_\mathcal{N} + \mathcal{P}_{ext} \qquad \mathcal{P}_\mathcal{N} := \mathcal{P}_\delta + \mathcal{P}(\delta \boldsymbol{u}) \tag{11}$$

where $\mathcal{E}_M$ is the mechanical energy of the particle system, formed by kinetic energy $\mathcal{E}_K$ and potential energy $\mathcal{E}_P$. The elastic potential energy $\mathcal{E}_C$ is defined as:

$$\mathcal{E}_C \;=\; \mathcal{E}_C(\rho_0) \;+\; c_0^2 \sum_i \left(\log \frac{\rho_i}{\rho_0} \;+\; \frac{\rho_0}{\rho_i} \;-\; 1 \right) m_i \tag{12}$$

where the state equation (3) has been considered and $\mathcal{E}_C(\rho_0)$ is the internal energy at rest (*i.e.* $\rho = \rho_0$). Within the weakly compressible regime, the elastic energy term $\mathcal{E}_C$ is generally negligible in the energy balance; hence it is not considered in the following discussion.

The external power $\mathcal{P}_{ext}$ exerted by the tank walls on the fluid is evaluated through the mutual interaction between fluid and solid particles, as detailed in Antuono *et al.*[60] and in Cercos-Pita *et al.*[61]. The power related to the viscous forces is directly evaluated through the expressions (8) as:

$$\mathcal{P}_V + \mathcal{P}_V^{turb} = \frac{K}{2} \sum_i \sum_j (\; \mu + \mu_{ij}^T \;)\; \pi_{ij}\; \boldsymbol{u}_{ij} \cdot \nabla_i W_{ij}\; V_i\; V_j \tag{13}$$

where the quantity $\mathcal{P}_V^{turb}$ refers to the viscous dissipation of the modelled sub-grid scales, whereas $\mathcal{P}_V$ refers to the resolved scales. Finally, the term $\mathcal{P}_N$ takes into account the effect of the density diffusion $\mathcal{P}_\delta$ (see Meringolo *et al.*[47]):

$$\mathcal{P}_\delta \;=\; \sum_i \frac{p_i}{\rho_i} \sum_j \delta_{ij}\, \boldsymbol{\psi}_{ij} \cdot \nabla_i W_{ij}\, V_i\, V_j \tag{14}$$

and the effect related to the particle shifting $\delta \boldsymbol{u}$, *i.e.* $\mathcal{P}(\delta \boldsymbol{u})$. Both these terms are linked to the stability of the scheme and are both included in $\mathcal{P}_N$, likewise a numerical diffusion term. Finally, the discrete form of the energy dissipated, $\mathcal{E}_{diss}$, can be expressed as:

$$\mathcal{E}_{diss} = \int_{t_0}^{t} \mathcal{P}_{diss}\ dt, \qquad \mathcal{P}_{diss} := \mathcal{P}_V + \mathcal{P}_V^{turb} + \mathcal{P}_N \tag{15}$$

where t_0 is the initial time instant of the simulation.

During the impacts energy losses occur, therefore the weakly-compressible approach acts in such a way that acoustic waves, coming from the conversion of mechanical energy and travelling at velocity c_0, are formed and then dissipated through the density diffusion term, *i.e.* $\mathcal{P}_\delta$, as investigated in Meringolo *et al.*[47].

When no impacts occur and vortices are generated during post-impact events, the mechanical energy is mainly dissipated by the viscous terms ($\mathcal{P}_V + \mathcal{P}_V^{turb}$) rather than by $\mathcal{P}_\delta$. However, by increasing the spatial resolution both $\mathcal{P}_N$ and $\mathcal{P}_V^{turb}$ decrease, whereas $\mathcal{P}_V$ increases. Indeed, as suggested by Pope[62], for a good LES simulation the resolved turbulent kinetic energy should be greater than the energy associated to eddy viscosity. Therefore, the power associated to real viscosity $\mathcal{P}_V$ (which depends upon the resolved velocity gradients) should be greater than $\mathcal{P}_N$ and $\mathcal{P}_V^{turb}$. It is worth noting that even in the discrete form $\mathcal{E}_C$, $\mathcal{P}_V$, $\mathcal{P}_V^{turb}$ and $\mathcal{P}_\delta$ are invariant under coordinate changes from inertial to non-inertial reference frame.

Finally, integrating in time the energy balance (11) between the time instants t_0 and t we obtain:

$$\mathcal{E}_M(t) - \mathcal{E}_M(t_0) = \mathcal{W}_{ext} + \mathcal{E}_{diss}, \qquad \mathcal{W}_{ext} := -\int_{t_0}^{t} F_z(t)\, v_{tank}(t)\ dt \tag{16}$$

where F_z is the vertical force exerted by the liquid on the tank and v_{tank} the vertical velocity of the tank. By subtracting the inertial term from F_z, the force F_z^{dyn} linked to the deformation of the liquid inside the tank is obtained:

$$F_z^{dyn}(t) := F_z(t) - M_{liquid}\,[-g - a_{tank}(t)] \tag{17}$$

with M_{liquid} the mass of the liquid contained in the tank and a_{tank} the vertical tank acceleration. According to such a decomposition, the energy balance can be rewritten as:

$$\begin{cases} [\mathcal{E}_M(t) - \mathcal{E}_M^{stat}(t)] - [\mathcal{E}_M(t_0) - \mathcal{E}_M^{stat}(t_0)] = \mathcal{W}_{ext}^{dyn} + \mathcal{E}_{diss}, \\ \mathcal{W}_{ext}^{dyn} := -\displaystyle\int_{t_0}^{t} F_z^{dyn}(t)\, v_{tank}(t)\ dt, \qquad \mathcal{E}_M^{stat} := M_{liquid}\left(\frac{1}{2} v_{tank}^2 + g\, z_{tank}\right) \end{cases} \tag{18}$$

where $\mathcal{E}_M^{stat}$ is the mechanical energy of liquid linked to the tank motion only. The term z_{tank} refers to the tank bottom vertical elevation from its initial position, where it is assumed $\mathcal{E}_M(t_0) = \mathcal{E}_M^{stat}(t_0)$. The dynamical work $\mathcal{W}_{ext}^{dyn}$ is the work related to the fluid domain deformation only, *i.e.* due to the sloshing motion. At the final time of the simulation t_f the liquid may be assumed at rest, so that the left-hand side of equation (18) becomes negligible and it follows that:

$$\mathcal{E}_{diss}(t_f) = -\mathcal{W}_{ext}^{dyn}(t_f) \tag{19}$$

From this relation it results that from the measure of the force F_z on the tank and its velocity v_{tank} it is possible to evaluate the experimental dynamical work $\mathcal{W}_{ext}^{dyn}$ and therefore the liquid dissipation $\mathcal{E}_{diss}(t_f)$.

VI. NUMERICAL RESULTS

In this section the law of motion resulting from the experiment of Martinez-Carrascal and González-Gutiérrez[29] is imposed on the tank. The law of motion presents an exponential decay due to the energy that is quickly dissipated by the liquid, and to a lesser extent, by the springs and the supporting rails.

In addition to the study of the energy dissipation under decaying motion, this test case allows for a comparison of the obtained forces (and related work) acting on the tank with those recorded in the experiment. The maximum amplitude of the oscillation motion, taken from recordings in the experiment, is $2A/L = 1.14$. The frequency of motion is defined as $f_0 = \sqrt{k/m} \ / \ 2\pi = 6.51$ Hz, where k is the spring stiffness and m the sum of the masses of the tank, the liquid and the springs. The period $T = 1/f_0 = 0.154$s is assumed as the reference time scale. The reference velocity is $U_{max} = 2\pi A/T = 2.33$ m/s. The corresponding Reynolds number depends on the fluid tested: for the water Re = 233,000, whereas for the oil it is 4,660.

In figures 3 and 4 the recorded motion of the tank is plotted in terms of, respectively, elevation and acceleration of the tank considering both water and oil. When the tank is filled with water the motion is more rapidly damped with respect to the oil case. This is inline with the analysis performed in Bouscasse *et al.*[22] and is linked with the higher fragmentation phenomena, occurring at higher Reynolds number, which induce a larger fluid energy dissipation. In figure 4 the portion of the time evolution for which the flow is

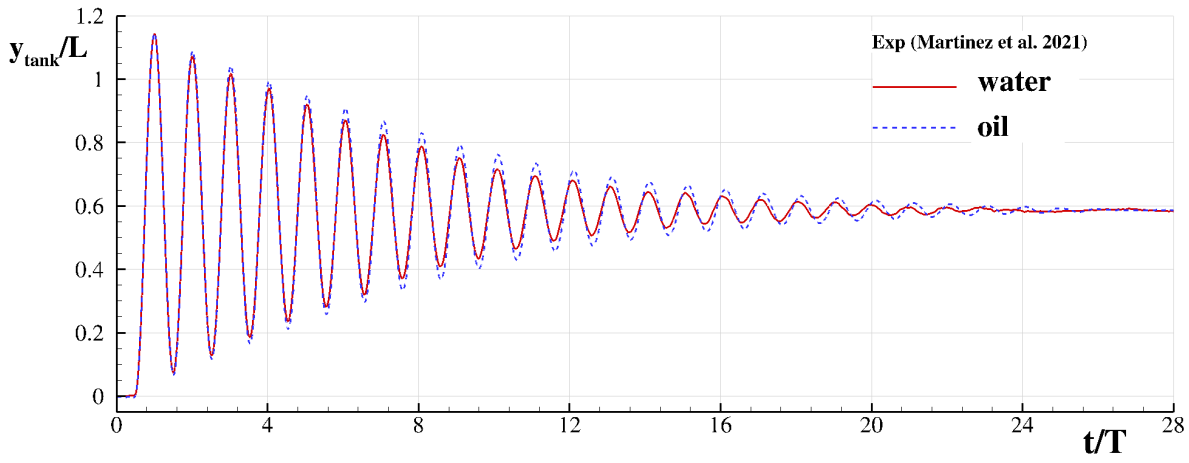

Figure 3. Tank motion recorded in the experiment of Martinez-Carrascal and González-Gutiérrez[29]: tank with water (solid line) tank with oil (dashed line).

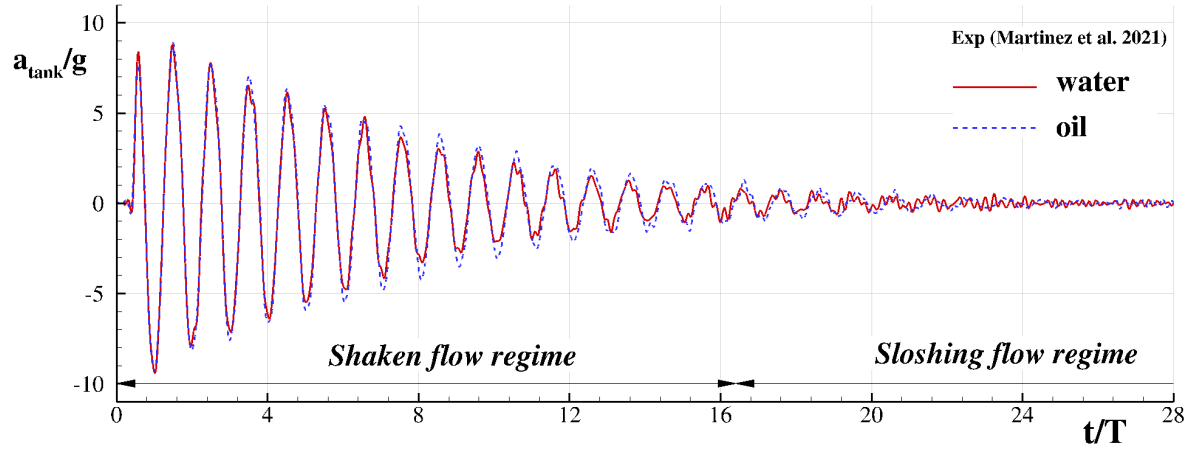

Figure 4. Tank acceleration recorded in the experiment of Martinez-Carrascal and González-Gutiérrez[29]: tank with water (solid line) tank with oil (dashed line).

in the "shaken flow" regime is highlighted. According to Marrone *et al.*[32,33], the "sloshing" regime is assumed to be attained when $a_{tank}/g \leq 1$, where a_{tank} is the tank acceleration. The maximum acceleration reached during the experiment is close to 10g which is of the same order of magnitude as limit design cases of an airliner wing during a wind gust Gambioli *et al.*[63].

The resolution is the same for both cases with $N = 75 = H/\Delta r$ the discretization of the liquid depth at rest, so that the final number of particles is about 2.8 million. The adopted speed of sound is $c_0 = 40$ m/s resulting in an initial time step $\Delta t = 20\,\mu s$. However, during

the simulation the time step decreases due to the constraint Δt_a in equation (10) resulting, at the end of the simulation, in a total number of iteration of about $350,000$. This large number is the main reason for the challenging computational cost of these simulations although the number of particles may not appear to be so large (see also Pilloton *et al.*[64]).

A. Flow field comparisons

In this section the results obtained from 3D simulations for both oil and water cases are discussed. The same results are also compared to the outcomes of the 2D simulations from Marrone *et al.*[33]. In figures 5 and 7 the vortex structures of oil simulations are depicted along with the vorticity fields obtained from 2D simulations at the same simulation time. The 3D vortex structures are identified through the Q-criterion calculated as:

$$Q = \frac{\mathbb{W}^2 - \mathbb{D}^2}{2} \tag{20}$$

where $\mathbb{W}$ is the spin tensor, *i.e* the anti-symmetric part of the velocity gradient tensor. Specifically, iso-surfaces with Q=50 are depicted. For the sake of clarity the 3D free-surface is made transparent. A rendering of the free surface for the first two time instants is provided at the bottom of figure 5. In figures 6 and 8 the same is reported for the water test case.

The 3D flow evolves similarly to the 2D one discussed in Marrone *et al.*[33]: in the initial stage, during the first upward acceleration of the tank, a small free-surface wave is generated due to the collapse of the menisci at the lateral walls. The waves travel from the lateral walls towards the centre of the tank. When the tank inverts its acceleration direction for the first time, a Rayleigh-Taylor instability is triggered. The inception of this instability starts from the small gravity waves generated by the menisci collapse. The fluid viscosity plays a significant role in the intensity of this first impact.

As shown in figure 5, for the oil case in 2D (top-right plot) two main thin jets moving towards the tank ceiling are discernible close to the lateral walls; similarly, in 3D (top-left and bottom-left plot) a thin film of fluid moves, parallel to the lateral walls, towards the tank ceiling. The water case, shown in figure 6, is clearly more energetic as a large part of the fluid in the middle of the tank moves upward. In 2D the rising fluid is essentially distributed onto the main diverging jets, with several other smaller jets ejected at the same time. In 3D the moving liquid forms four main jets corresponding to the four tank corners. The small

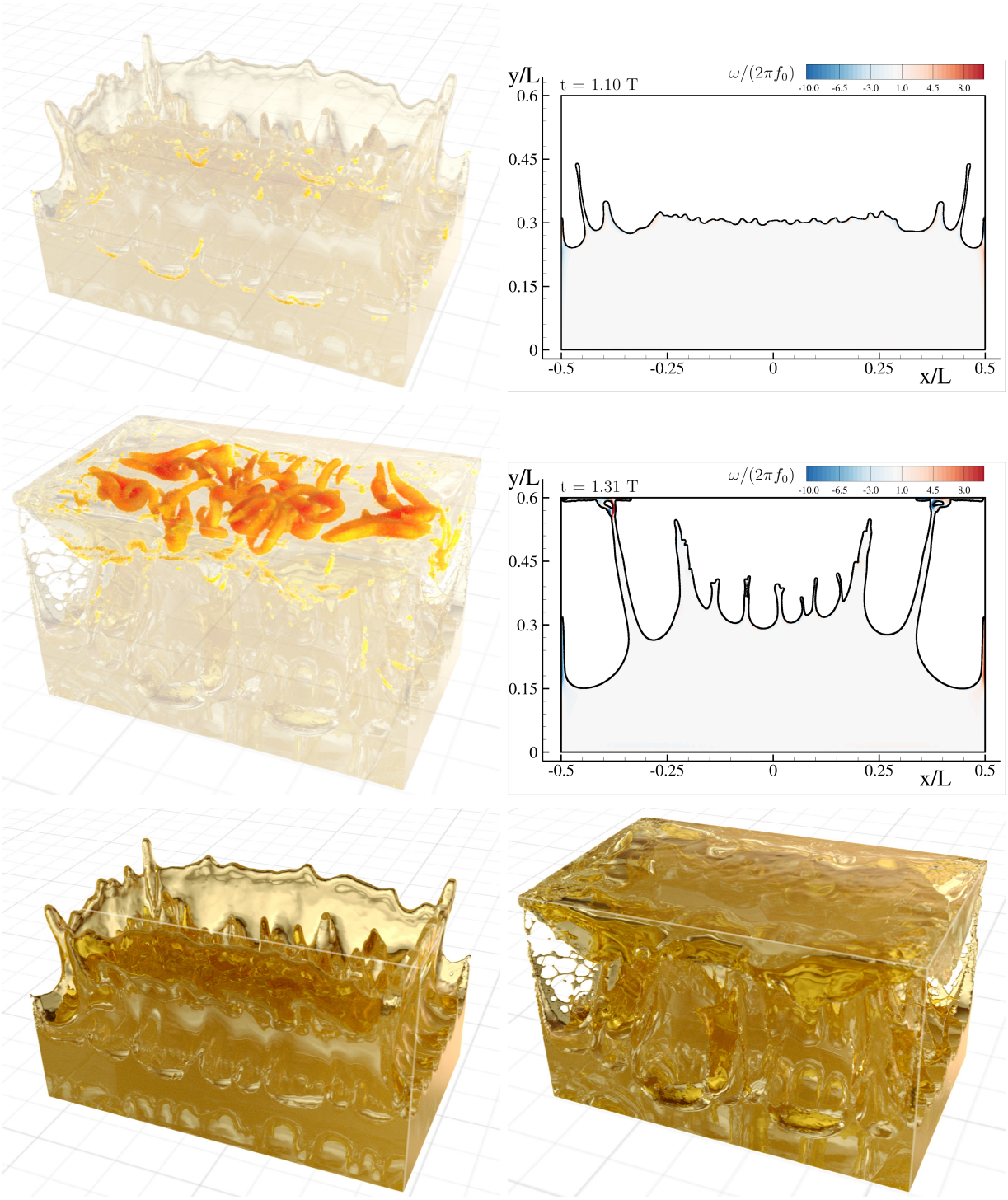

Figure 5. Top, middle: comparisons between 3D (**left**) and 2D (**right**) simulations of oil sloshing. In 3D the iso-Q surfaces for $Q = 50$ are plotted against the vorticity in 2D. Bottom: rendering of the free surface at the same time instants. Low resolution videos are available as supplementary material (Multimedia view).

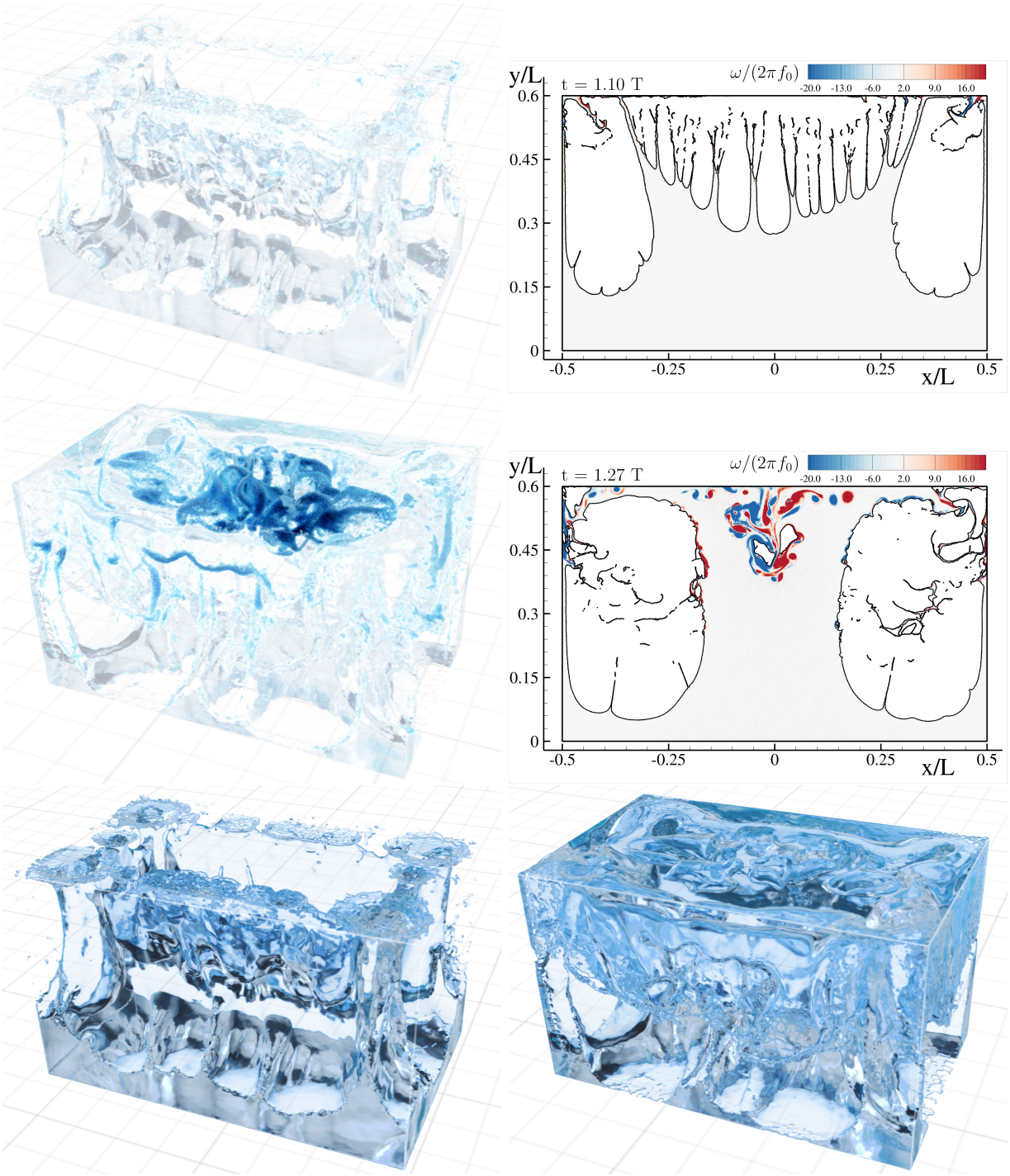

Figure 6. Top, middle: comparisons between 3D (**left**) and 2D (**right**) simulations of water sloshing. In 3D the iso-Q surfaces for $Q = 50$ are plotted against the vorticity in 2D. Bottom: rendering of the free surface at the same time instants. Low resolution videos are available as supplementary material (Multimedia view).

structures observed in 2D are not visible in this case as the resolution is significantly coarser

($N = 400$ versus $N = 75$).

When the fluid impacts the ceiling (middle plots and bottom-right plot of figures 5 and 6), the different flow dynamics explained above induce different types of impacts: in the oil case when the jets impact the ceiling the rectangular film expands over the ceiling and produces large and tangled vortex tubes occupying a large region of the tank wall; in the water case a larger amount of liquid impacts slightly in advance with respect to the oil case. This generates a pocket at the centre of the tank ceiling enclosing the vortex structures generated by the previous impingement of the liquid jets. The 2D evolution for water is quite similar to its 3D counterpart, whereas for the oil the impact is not complete at the

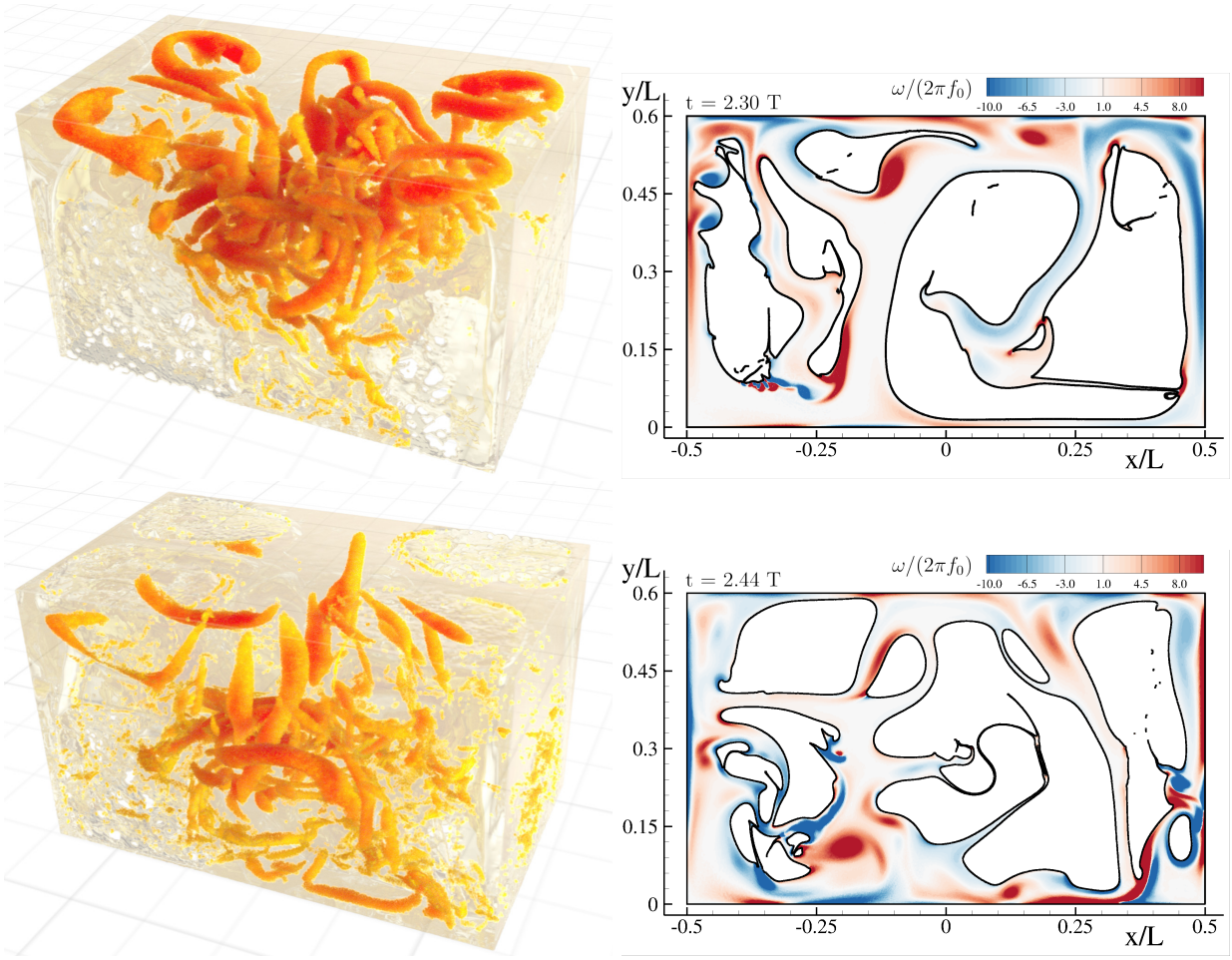

Figure 7. Comparisons between 3D (**left**) and 2D (**right**) simulations of oil sloshing. In 3D the iso-Q surfaces for $Q = 50$ are plotted against the vorticity in 2D. The corresponding times of 2D simulations are reported at the top left of the corresponding frame. Low resolution videos are available as supplementary material (Multimedia view).

same simulation time and only the impinging of the two initial jets occurs (see middle right plot of figure 5). After the first impact, the fluid starts a series of cyclical impacts against the ceiling and the floor of the tank. As shown in figure 7 and 8, in 2D the fluid is mostly fragmented in multiple jets and the energy is dissipated in free-surface re-connections and the consequent generation of vorticity. Lower viscosity is associated to thinner jets and a larger number of vortices, as visible in the water vorticity fields shown in the right column of figure 8. Conversely, the oil case is characterised by thicker jets and the liquid covers almost the entire solid surface.

In the 3D simulations a proliferation of vortex tubes during the impacts is observed.

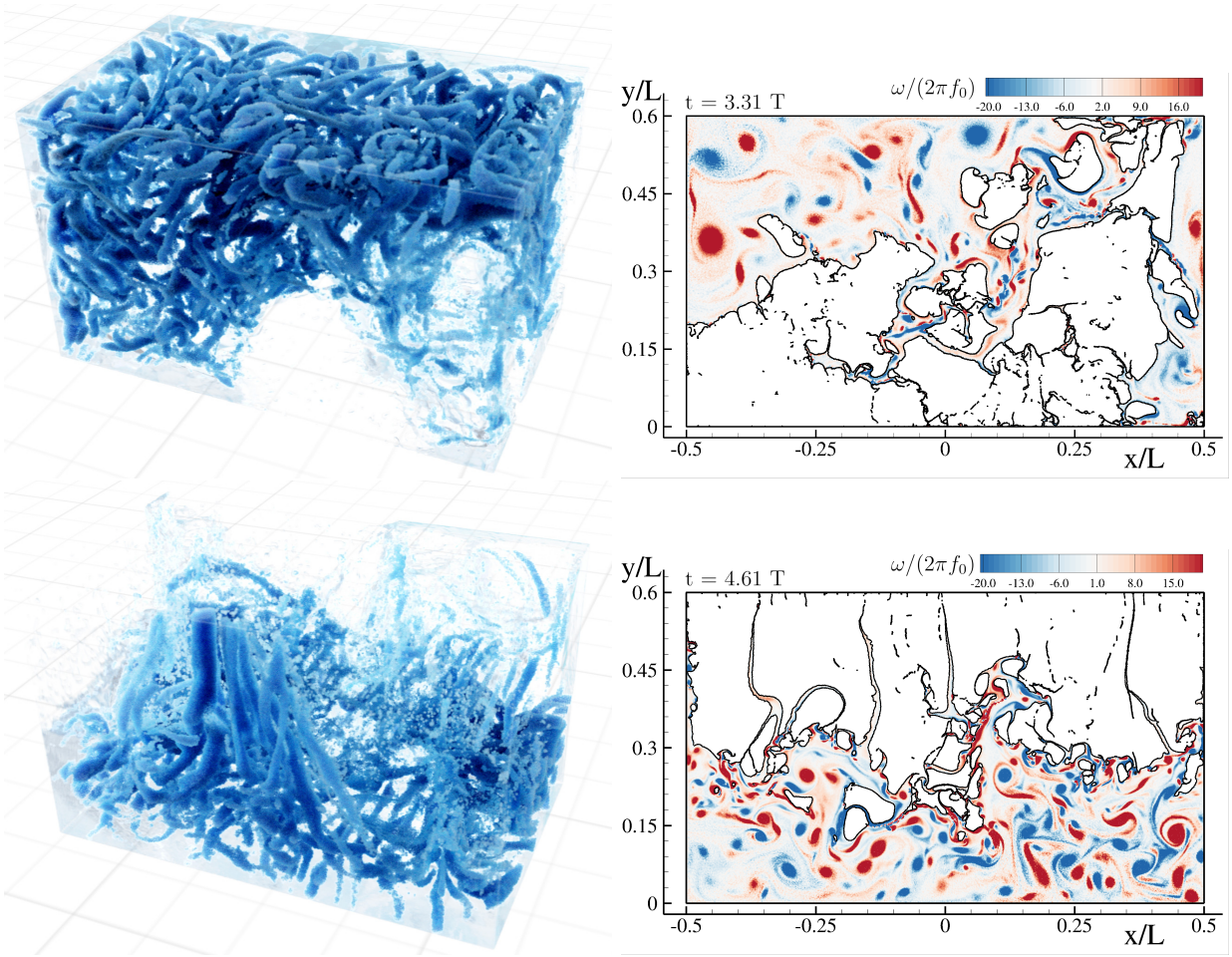

Figure 8. Comparisons between 3D (**left**) and 2D (**right**) simulations of water sloshing. In 3D the iso-Q surfaces for $Q = 50$ are plotted against the vorticity in 2D. The corresponding times of 2D simulations are reported at the top left of the corresponding frame. Low resolution videos are available as supplementary material (Multimedia view).

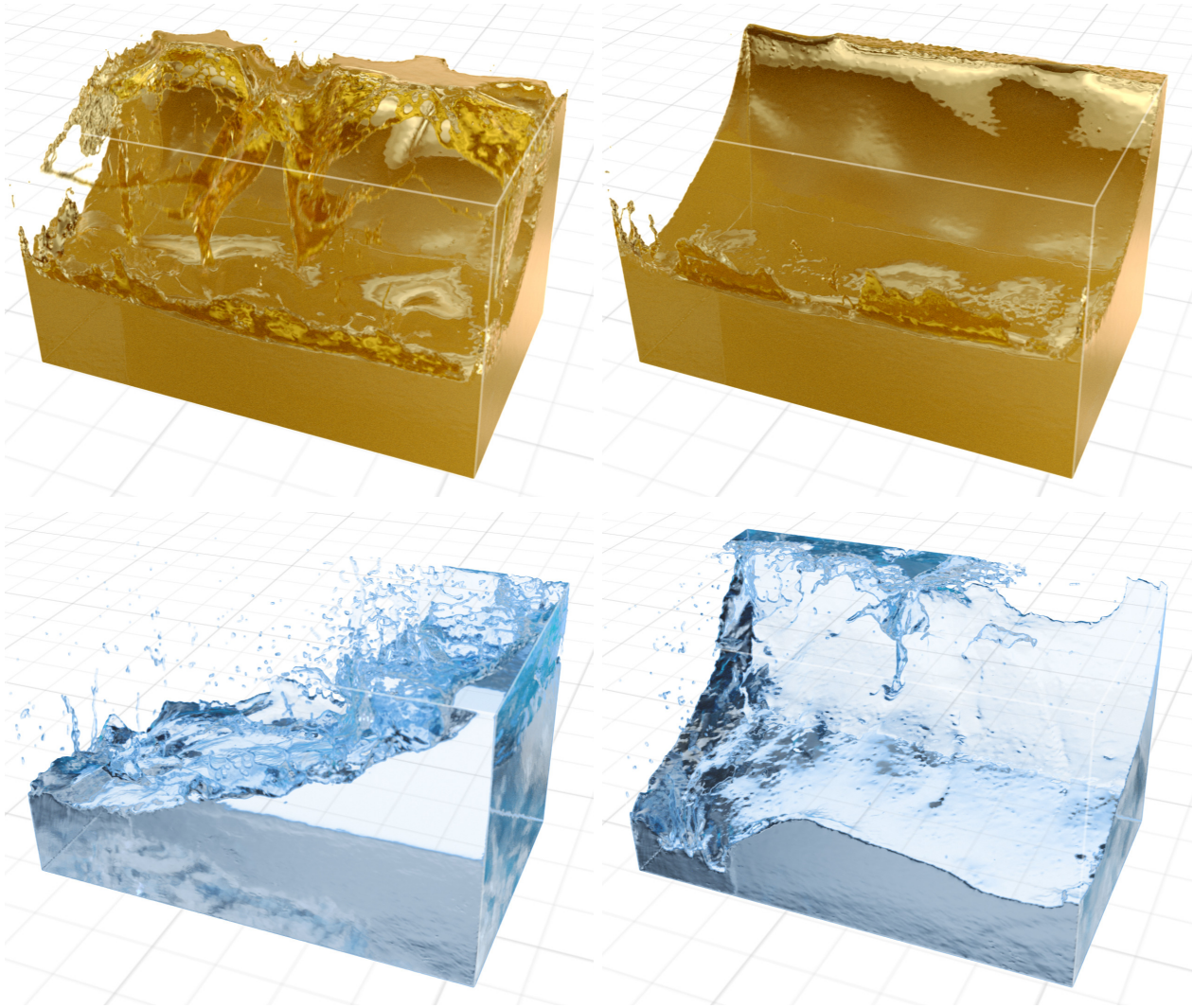

Figure 9. Comparisons between rendered free surfaces of oil (**top**) and water (**bottom**) sloshing for later times. On the **left** column $t = 16.5T$, on the **right** $t = 20T$.

This is particularly evident for the water case (left column of figure 8) in which highly entangled vortex structurs are spread all over the liquid domain at the impact instant. On the other hand, higher viscosity levels correspond to a smaller number of vortex tubes, mostly characterised by larger diameter size (left column of figure 7). When the transition from the "shaken" flow regime to the "sloshing flow" regime occurs, as explained in Marrone *et al.*[33], the flow is still highly fragmented with vorticity distributed on a wide range of length scales. Afterwards, the fluid regains its initial compact shape with gravity waves travelling over the liquid surface and impacting against the lateral walls and, occasionally, the tank ceiling. On the left column of figure 9 a time instant close to the transition from shaking to sloshing is

depicted for both oil and water. At this stage of the flow the vorticity content is very low and, therefore, it was chosen to plot only the free surface.

On the right column of figure 9 a time instant for which the sloshing regime is fully attained is shown: for the water case a weak swirling motion is also observed (see also Faltinsen and Timokha[2]). The latter induces a sloshing flow component also across the length of the tank (*i.e.* the x direction) whereas the oil exhibits a sloshing wave only across the tank width (*i.e.* the y direction).

1. Pressure field evolution

In this section the flow evolution is studied by considering the computed pressure fields. In figure 10 the numerical pressure fields are reported for the initial stage of the oil sloshing in 2D and in two orthogonal centre slices in 3D. At time $t = 1.00T$ the tank reaches its maximum vertical position and the tank acceleration is at its lowest value equal to $-9.3g$. As a consequence, the pressure field is characterised by a large negative "*hydrostatic*" component $\rho\,(a_{tank} + g)\,y$ with a value on the tank bottom of about $-8.3\rho\,g\,H$. When such a negative pressure value is reached the classic SPH model may suffer from the development of numerical instability, known as tensile instability. The appearance of this instability causes the fluid to numerically cavitate causing an unphysical sudden detachment from the tank bottom (see[32] for a detailed discussion). Conversely, in the present model the tensile instability is controlled through the adoption of the PST described in section III, thus avoiding such a significant drawback. After that, at $t = 1.15T$ the negative pressure component significantly decreases as the fluid is ejected towards the tank roof. In the 3D simulation the fluid ejection is anticipated with respect to 2D since in the former case the flow instability is triggered earlier. When the rising liquid sheet impacts the roof positive pressure peaks of about $8\,\rho\,g\,H$ are observed.

During the subsequent impact events, the pressure peaks reach higher values, as reported in figure 11, where the impact at $t = 2.56T$ at the bottom causes pressure levels of about $40\rho\,g\,H$. At this stage the flow configuration is quite complex and, consequently, the pressure distribution is heterogeneous across the fluid domain. At the end of the simulation $t = 26.25T$ when a smooth sloshing regime is attained, the pressure field is again close to the expected values of the hydrostatic distribution $\rho\,g\,H$. A similar behaviour in terms of evolution and

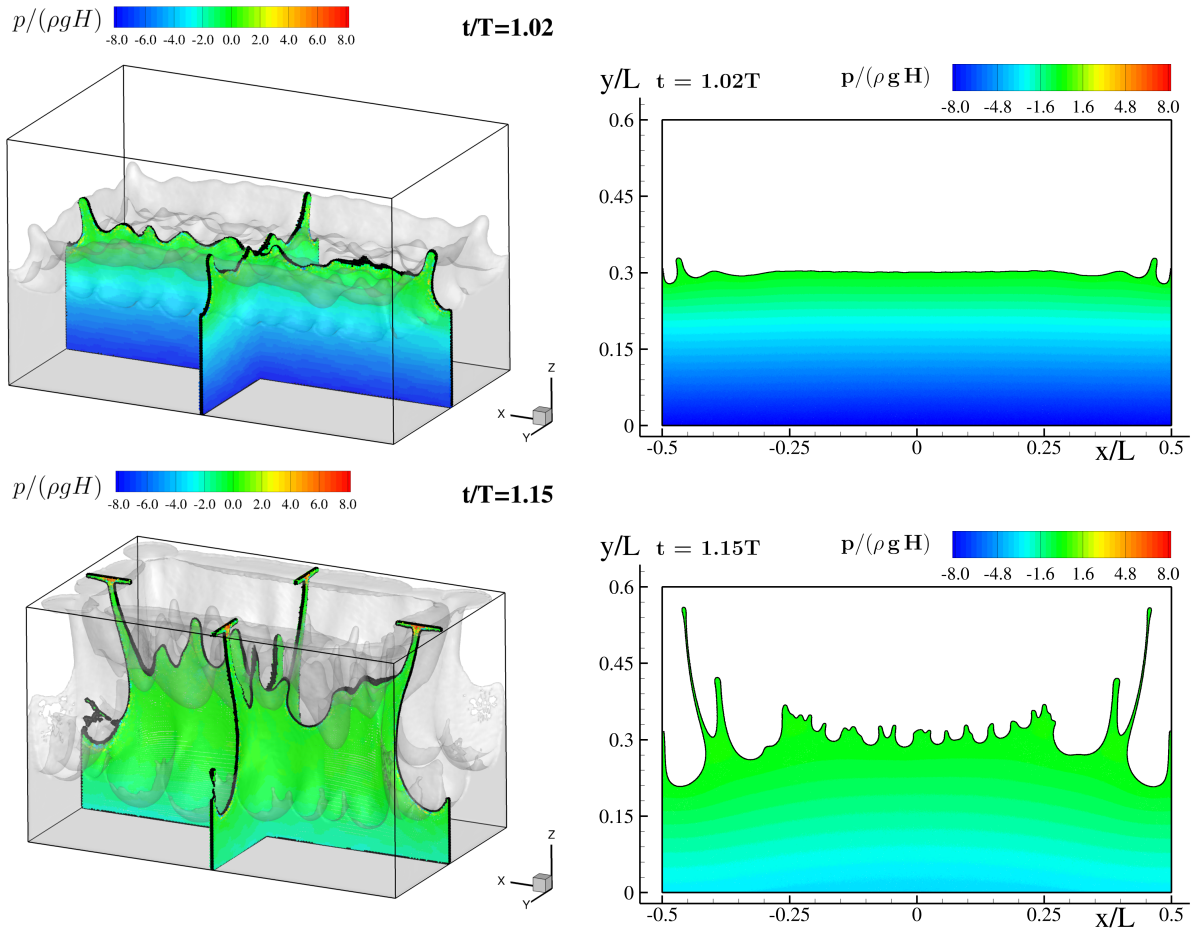

Figure 10. Comparisons between 3D (**left**) and 2D (**right**) pressure field for oil sloshing at the initial stage of the flow evolution: time $t = 1.02T$ (top row) and $t = 1.15T$ (bottom row).

values of the pressure field is found also for the water simulation which is not reported here for the sake of brevity.

B. Discussion of the energy dissipation

In this section the dissipated energy predicted by the numerical solver is analysed and compared to experimental data. In figure 12 the dissipated energy, $\mathcal{E}_{diss}$ (see eq. (15)), computed by SPH is plotted against the non-dimensional time for four different spatial resolutions varying from $N = 22$ to $N = 75$. A 1.5 ratio between two successive discretization levels was adopted. In the same figure the evaluation of the dynamical work done by solid walls in the experiments at the final time, $-\mathcal{W}_{ext}^{dyn}(t_f)$ (see eq. (18)), is also reported. As stressed in section V, the dynamical work is related to the fluid dissipated energy by relation

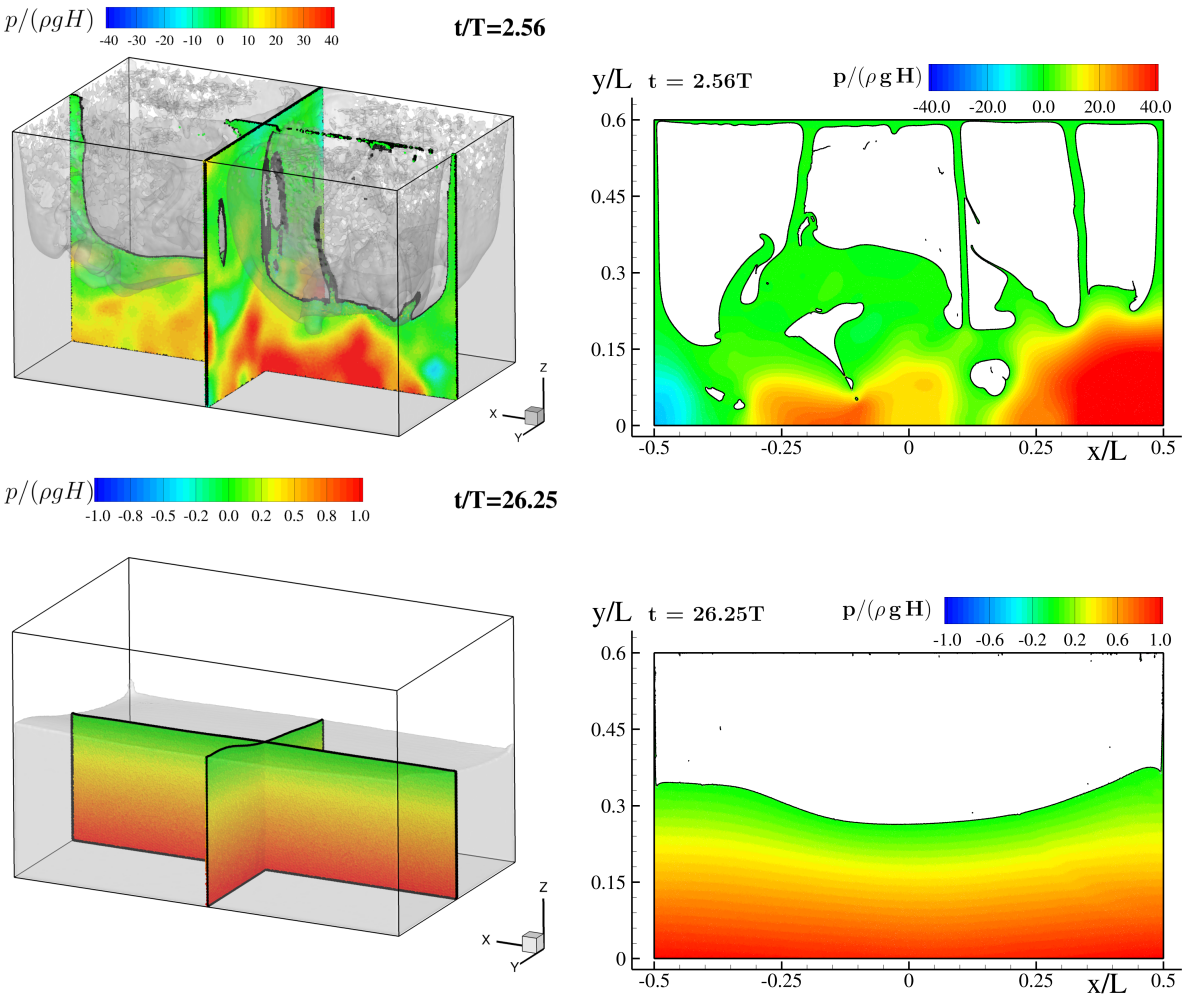

Figure 11. Comparisons between 3D (**left**) and 2D (**right**) pressure field for oil sloshing at time $t = 2.56T$ (top row) and at the end of the simulation $t = 26.25T$ (bottom row).

(19) where it is highlighted that $\mathcal{E}_{diss}$ and $-\mathcal{W}_{ext}^{dyn}$ are expected to be very close at the final stage of the simulation when the fluid is almost at rest. The dissipated energy is made non-dimensional by the potential energy $\Delta\mathcal{E} = \rho_W g\ LWH\ 2A = 0.201$ J for water and 0.181 J for oil.

In the left plot of figure 12 the convergence analysis of $\mathcal{E}_{diss}$ is shown for the oil test case. No significant variations are observed for the different resolutions: this suggests that even the lowest discretisation, $N = 22$, is sufficient to resolve the inertial range of the turbulent cascade. This aspect is further inspected in figure 13. The final value of $\mathcal{E}_{diss}$ is quite close to the experimental evaluation of $-\mathcal{W}_{ext}^{dyn}$.

For the water case, right plot of figure 12, the situation is significantly different:

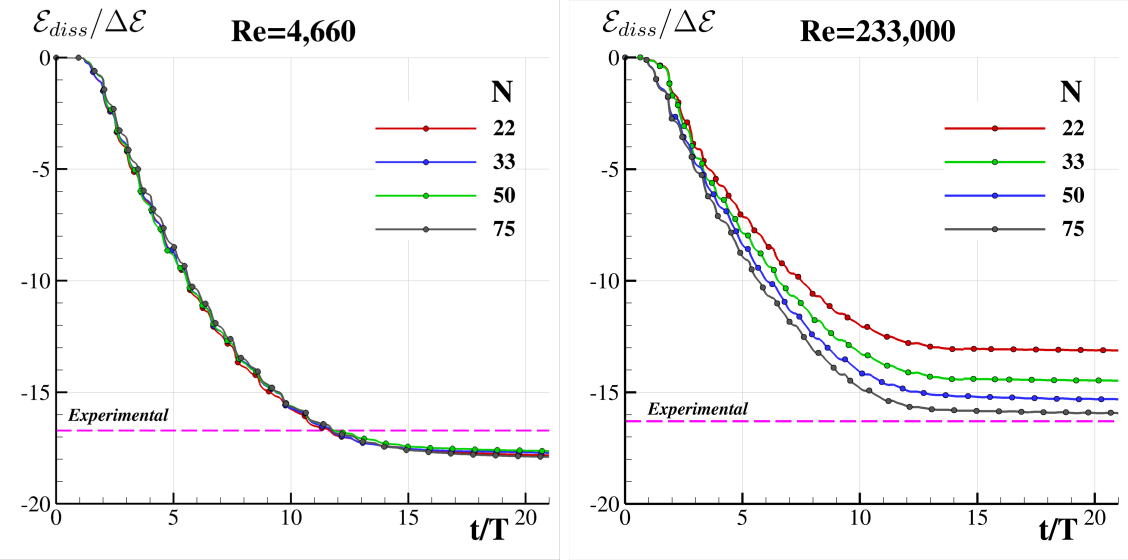

Figure 12. Convergence of the dissipated energy for oil (**left**) and water (**right**). With the dashed line, the experimental data obtained for $-\mathcal{W}_{ext}^{dyn}$ at final time, as shown in figure 17.

convergence of the dissipated energy is not attained for the considered resolutions. Even if the experimental value is close to the result at $N = 75$, it is expected that a further increase in the resolution will result in a larger value of the final dissipated energy. This aspect is further discussed later in the section. Beside the above observation, it is worth noting that the dependency on the spatial resolution is reduced when increasing it, even if the rate of convergence is still very low.

In figure 13 the different energy components specified by (15) are reported for both liquids and for the highest resolution $N = 75$. Even if, as already mentioned, the final values are very close to each other, the various contributions are differently distributed. Considering that the resolution is the same, for the lower Reynolds number case the dissipation coming from the viscous terms of resolved scales is the most prominent contribution (accounting for about the 62%). Conversely, for the water case it accounts for about 5% of the total dissipation. This difference is to be ascribed to the resolution adopted, which is sufficient to describe correctly the energy dissipated by the viscous terms in the inertial range only at the Reynolds regime of the oil.

Coherently, the contribution from the sub-grid scales, $\mathcal{E}_V^{turb}$ significantly exceeds the others in the water case, where it amounts to 74% of the total dissipation. This is a typical clue of an incomplete description of the inertial range which results in a higher

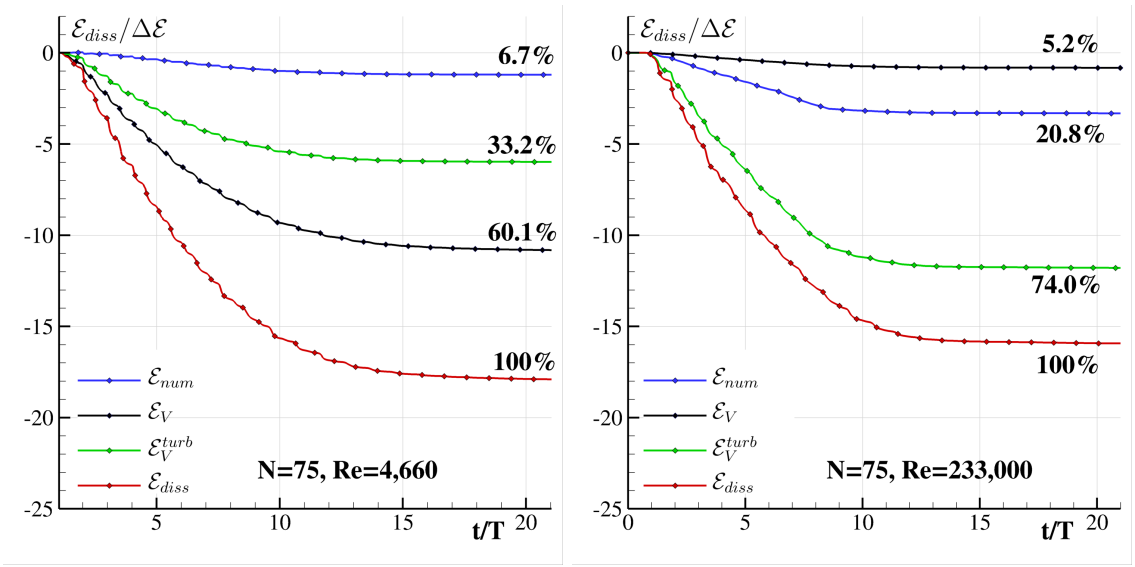

Figure 13. Time histories of the dissipated energy for oil (**left**) and water (**right**). The different components are highlighted and drawn with different line colors.

turbulent viscosity μ_T, depending on the local value of the velocity gradient $||\mathbb{D}||$. For the oil simulations the resolution is sufficient to have smooth local velocity gradients, thus limiting the contribution from modelled viscous stress to 33.2%. The dissipated energy related to numerical diffusion $\mathcal{E}_{num}$ follows the same behaviour as $\mathcal{E}_V^{turb}$.

In figure 14 the ratio between the turbulent and the fluid viscosity μ_T/μ is reported on a volume slice for both cases and two different resolutions. The fields are evaluated at t = 5.2T, where the flow is in the shaken regime. Considering the oil case (top plots), for the higher resolution the ratio is lower than 0.5 almost everywhere, thus indicating that the sub grid scales are well modelled and that the inertial range is correctly captured. Also in the coarser case the ratio does not exceed 5.0, which is still a good value for a well resolved LES simulation (Sagaut[65]).

Conversely, the turbulent viscosity largely exceeds the fluid one for the water case even at the highest resolution N = 75: the observed values are around $\mu_T/\mu \approx 30$, whereas for a good LES the ratio should be of order $\mathcal{O}(1)$ (Sagaut[65]). For coarser resolution the sub-grid scales are, *a fortiori*, not adequately modelled and the cut-off of the energy exchange takes place within the inertial range (Aprovitola and Denaro[66]). These aspects provide further elements for the discussion of the convergence analysis in figure 12: it can be easily concluded that for the water test case the highest resolution is still too coarse to obtain a convergent

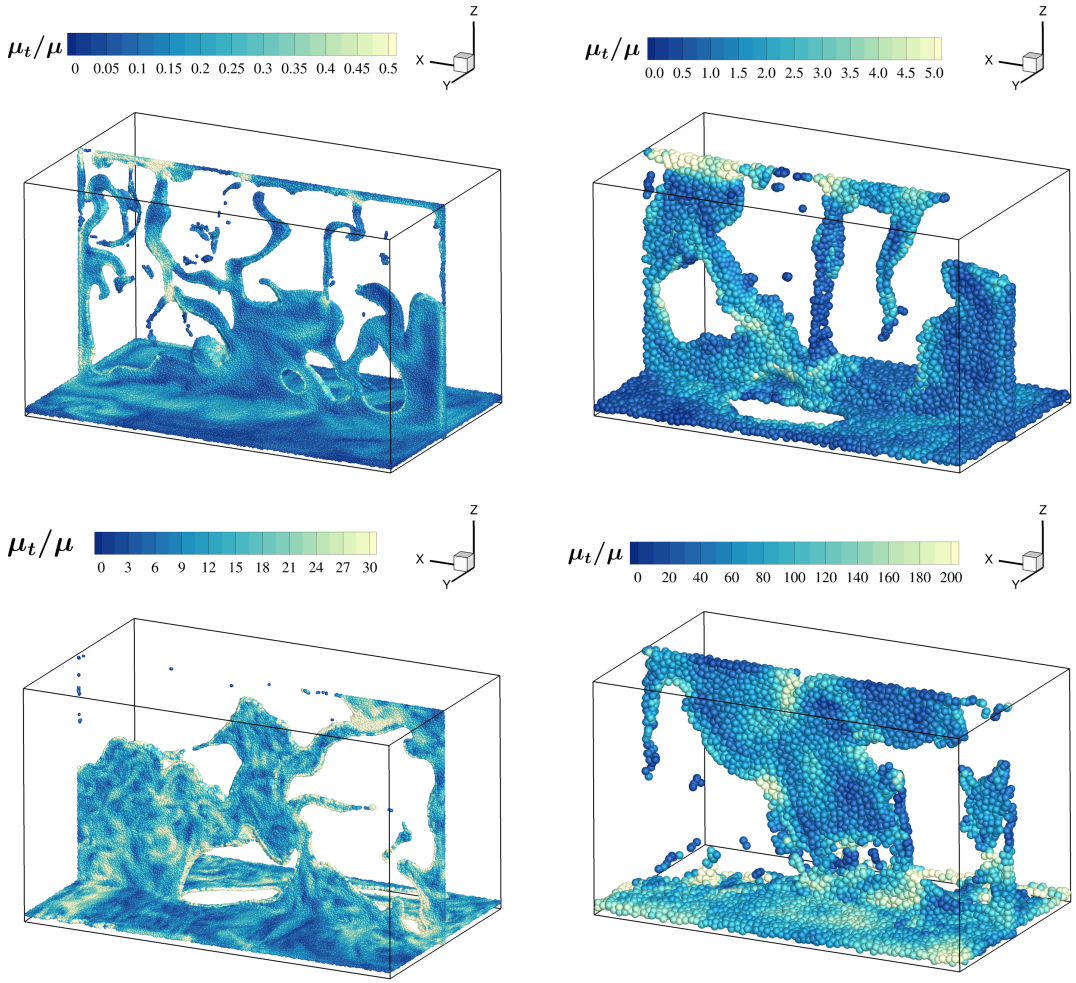

Figure 14. Slice of μ^T/μ for the oil (**top**) and water (**bottom**) simulations with different resolutions. On the **left** the finer resolutions, on the **right** the coarser ones.

result. Regarding this topic, in Marrone *et al.*[33] an in-depth study was performed in the 2D framework.

Although in 2D the effect of the vorticity is more intense and a direct comparison with 3D is not possible, in the former work it was observed that a result close to a convergent limit was obtained at Re=233,000 with a spatial resolution as high as $N = 400$. In that case the observed maximum ratio was $\mu_T/\mu = 5$ (shown in figure 15 at time t/T=4.55). Such a resolution in 3D corresponds to about 430 million of particles and 425 days of computing time on 1000 cluster cores.

In figure 16, the comparison between the vertical force acting on the box coming from the 2D, 3D simulations and experiments is reported. Note that the total weight of the liquid

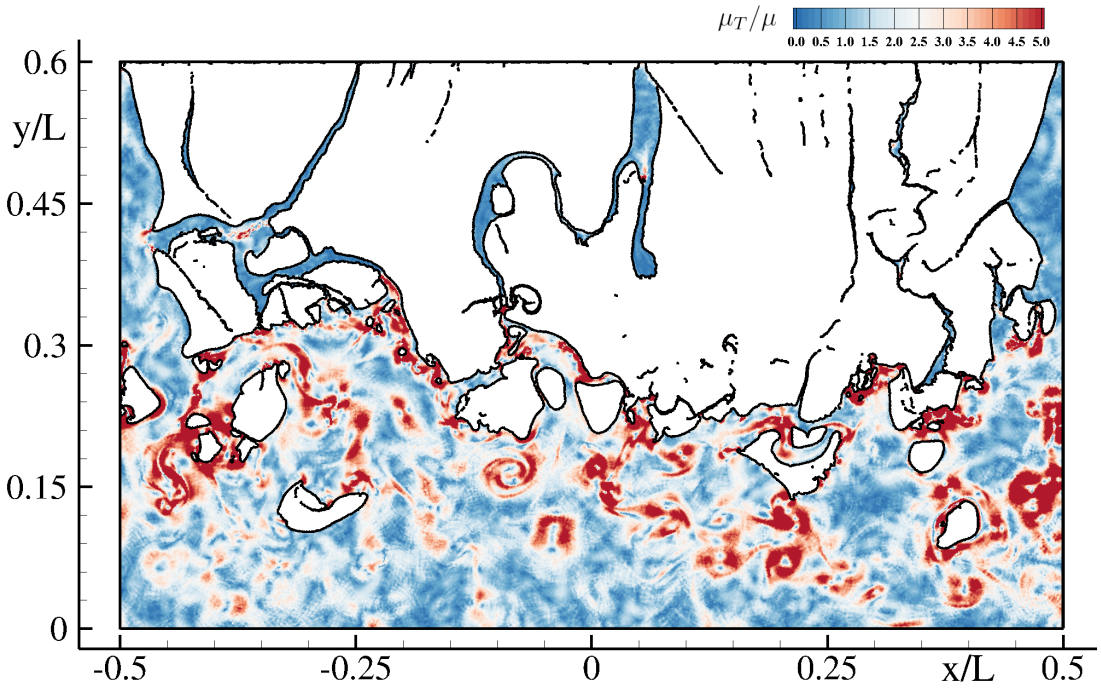

Figure 15. μ_T/μ ratio distribution for the 2D case at Re=233,000 using a spatial resolution N=400 (Marrone *et al.*[33]).

mass $\rho gLWH$ has been subtracted from the vertical force, so that a null force is measured when the tank is at rest. As highlighted in Martinez-Carrascal and González-Gutiérrez[29] and in Marrone *et al.*[33], before and during the first impact an unphysical overshoot of the force is recorded in the experiments. This is related to incorrect load cell measurements and caused by the release mechanism. For ease of discussion in the present work that part of the experimental recording has been removed and only the later stage of the evolution is considered for comparison hereinafter.

For the water case the 2D and 3D results are rather similar, although the resolutions for the two approaches are significantly different (*i.e.* $N = 400$ versus $N = 75$). Conversely, for the oil case the force predicted in 2D underestimated the 3D force, and this is mainly linked to effects of the boundary layer region on whole walls of the 3D box. For both water and oil the force peaks are better resolved in the 3D solution with respect to its 2D counterpart in which they are rather smoothed. The predicted forces in 3D are, generally, in good agreement with the experimental data and follow quite closely the damped oscillations of the vertical force on the box.

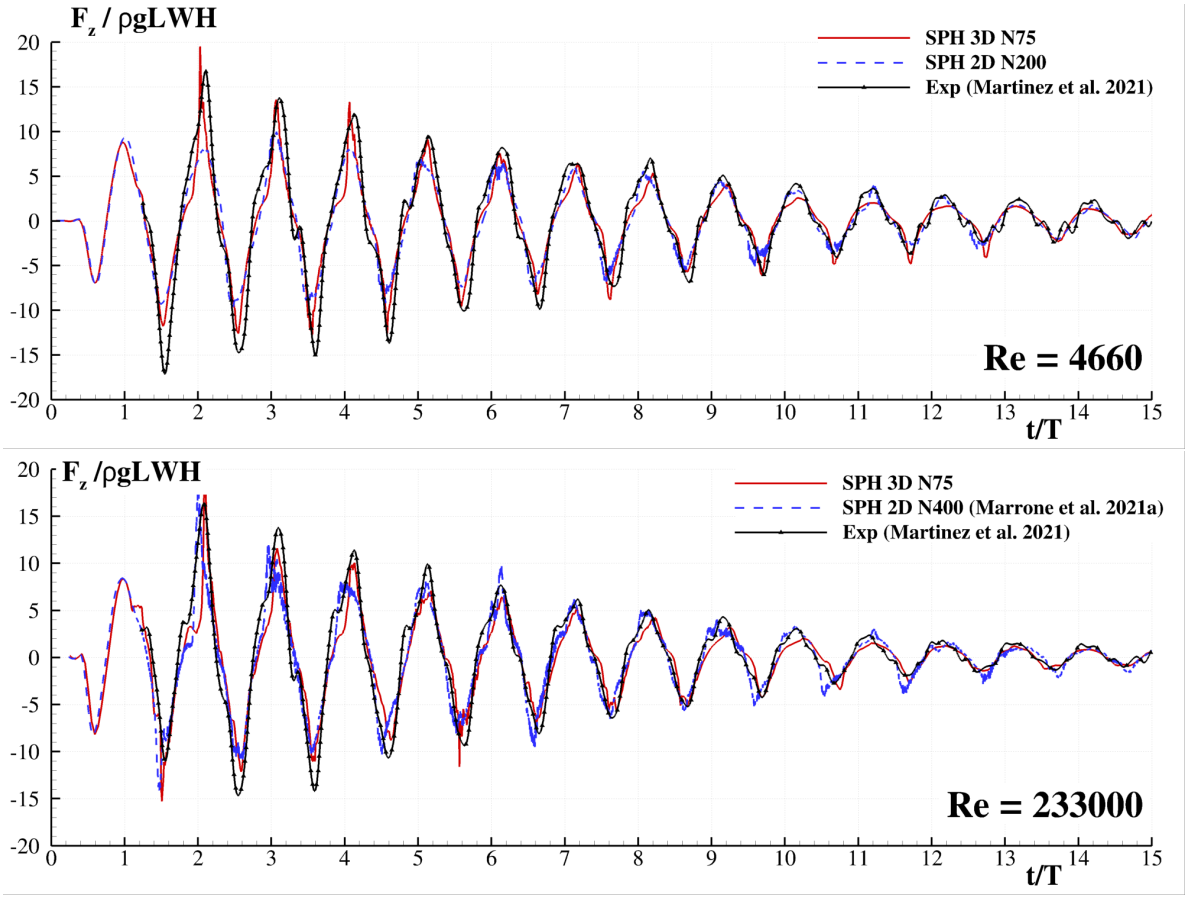

Figure 16. Time histories of the vertical force on the box compared with the 2D and experimental outcomes of Martinez-Carrascal and González-Gutiérrez[29]. **Top** plot, the oil case; **bottom** plot, the water case.

In figure 17 the time histories of the dynamical work $-\mathcal{W}_{ext}^{dyn}$ defined in (18) are reported for both fluids. In the top plot of figure 17 the dynamical work for the oil is shown together with the experimental data by Martinez-Carrascal and González-Gutiérrez[29] and a 2D simulation at $N = 200$. The comparison shows a fair agreement between the numerical solution and the experiments. The 3D solution after an initial overlapping with the experimental data, at around $t/T = 6$ slightly diverges and overestimates the dynamical work. On the other hand, the 2D solution underestimates the dynamical work during the entire time evolution. The final gap between the numerical outcomes and the experimental value is about 9% and 13% respectively for the 3D and the 2D solutions. As far as the water simulations are concerned, the dynamical work is reported in the bottom plot of figure 17. In this case too, the 3D solution is in better agreement with the experimental data than the

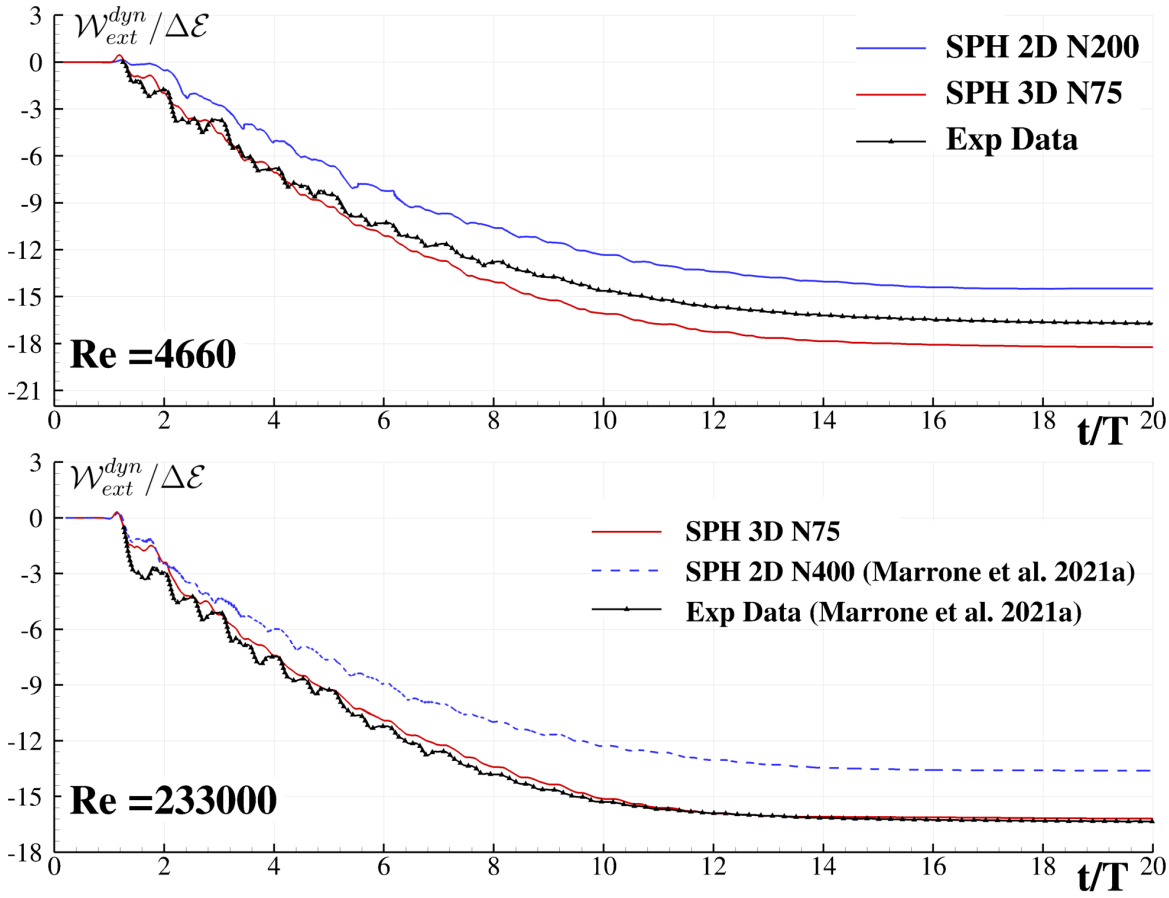

Figure 17. Time histories of the dynamical work compared with experiments and 2D simulations for oil (**top** plot) and water (**bottom** plot).

2D solution. However, it is important to recall that the resolution adopted for the water is not sufficient and, most likely, a further increase in the numerical resolution could lead to a different final value of the dissipated energy.

It is worth noting that the final value of $\mathcal{W}_{ext}^{dyn}$ observed in the 3D solutions is very close to the final value of $\mathcal{E}_{diss}$ for both water and oil cases. This is expected from eq. (19) but it is not a trivial result from a numerical point of view, as the two quantities are computed in very different ways: $\mathcal{E}_{diss}$ is measured during the simulation by means of eq. (15) while $\mathcal{W}_{ext}^{dyn}$ is computed *a posteriori* through eq. (18).

Summarising, the 3D simulations tend to overestimate the energy dissipation and this is probably linked to the role of the air phase which is neglected in the present work. In this regard, further investigations are needed. However, taking into account the air phase with an SPH model leads to a considerable increase in the CPU costs linked to the doubling of

the total number of particles and to a further reduction in the time step.

On the other hand, in order to obtain a more reliable validation procedure, further improvements are also needed from the experimental side. It is important to underline, indeed, that the experimental estimation of $\mathcal{W}_{ext}^{dyn}$ is challenging since even small time delays of a few milliseconds between the force and the tank velocity measurements may induce significant errors in the evaluation of the external work. Therefore, a sensitivity analysis targeting this specific quantity is needed in order to measure the uncertainty which affects the reference data.

C. CPU costs

In this subsection details on the CPU costs are given. The 3D simulation at highest resolution $N = H/\Delta r$=75 required 350,000 time iterations involving 2,800,000 particles with a kernel support containing an average number of 80 neighbours. This simulation ran for about 7 days using 240 cores on the Liger cluster machine in Ecole Centrale de Nantes which is equipped with 12-core Intel Xeon (Haswell) E5-2680v3 processors.

It is worth noting that those CPU costs are quite high since they are related to a research code which is not optimised for industrial applications. The high CPU costs are also related to the evaluation of the different energy components needed for the analysis presented in this work.

VII. CONCLUSIONS

In the present paper, the work of Marrone *et al.*[33] was extended to the 3D framework. Challenging numerical simulations of the violent sloshing flow in a moving tank were performed with specific focus on the prediction of the mechanical energy dissipated by the fluid during the motion. Two different Reynolds numbers, corresponding to oil and water, were considered and the numerical outcomes were compared to existing experimental data. The δ-LES-SPH approach was adopted and its capabilities in simulating these kinds of flows were discussed.

Three-dimensional features of the flow were observed and compared to previous 2D studies and experiments. As far as forces exerted by the fluids are concerned, the final 3D results

are generally closer to the experiments with respect to the highly resolved 2D simulations performed in Marrone *et al.*[33], in terms of both force peaks and overall envelop.

For the oil test-case we found that, as in 2D, a convergent result was reached, providing an overestimation of the energy dissipation of about 10% with respect to the reference experimental result. As for the water test-case, a fully converged solution was not reached due to the higher Reynolds number of the flow. However, comparing the numerical outcome to the reference experimental result an overestimation similar to the one obtained with oil is expected also for this case. Since the uncertainty of the experimental results was not quantified, it is difficult to assess an acceptable range of error as even small time errors between the force and the tank velocity measurements in the experiment may induce significant errors in the evaluation of the external work. To quantify more precisely the capability of the present model to tackle such problems, future studies using periodic sloshing motions should be considered such as the experimental campaign recently performed by Saltari *et al.*[67]. The use of a purely periodic motion would allow applying a statistical approach at the cost of a longer simulation time.

LIST OF SYMBOLS

C_S**:** Smagorinsky constant.

F_z^{dyn}**:** Vertical force exerted by the liquid on the tank without the inertial component.

F_z**:** Vertical component of the force exerted by the liquid on the tank.

H**:** Tank filling height.

L**:** Length of the tank and reference length of the problem.

N**:** Number of particles along the liquid depth at rest.

Q**:** Second invariant of velocity gradient tensor (Q-criterion vortex identification).

U_{max}**:** Maximum fluid speed.

V_i**:** Volume of $i-$th particle.

W_{ij}: Kernel function centered on particle i and related to particle j.

Δr: Average distance between particles.

Δt_a: Advective time step.

Δt_c: Acoustic time step.

Δt_v: Viscous time step.

Δt: Integration time step.

Ω: Fluid domain.

$\boldsymbol{F}_i^v$: Net viscous force acting on particle i.

$\boldsymbol{f}_{NI}$: Non-inertial accelerations.

$\boldsymbol{r}$: Material point position.

$\boldsymbol{u}$: Velocity field.

$\delta\boldsymbol{u}$: Particle shifting velocity field.

δ_{ij}: Intensity of the diffusion $\mathcal{D}^\rho$ between particles i and j.

$\mathcal{D}^\rho$: Diffusive term in the continuity equation.

$\mathcal{E}_C$: Elastic potential energy.

$\mathcal{E}_K$: Kinetic energy.

$\mathcal{E}_M$: Mechanical energy.

$\mathcal{E}_P$: Potential energy.

$\mathcal{E}_{diss}$: Dissipated energy.

$\mathcal{P}(\delta\boldsymbol{u})$: Power related to the Particle Shifting.

$\mathcal{P}_N$: Power related to numerical dissipation.

$\mathcal{P}_V^{turb}$: Power related to viscous dissipation of the sub-grid scales.

$\mathcal{P}_V$**:** Power related to viscous dissipation of the resolved scales.

$\mathcal{P}_\delta$**:** Power related to density diffusive term $\mathcal{D}^\rho$.

$\mathcal{P}_{diss}$**:** Dissipated power.

$\mathcal{P}_{ext}$**:** Power related to external forces.

$\mathcal{W}_{ext}^{dyn}$**:** Work of external forces related to fluid deformation only.

$\mathcal{W}_{ext}$**:** Work of external forces.

μ^T**:** Turbulent dynamic viscosity.

μ**:** Dynamic viscosity.

ν**:** Kinematic viscosity.

$\partial\Omega_B$**:** Body frontiers.

$\partial\Omega_F$**:** Free surface.

ρ_0**:** Fluid density at free-surface.

ρ**:** Fluid density.

σ**:** Surface tension.

$\mathbb{D}$**:** Rate of strain tensor, *i.e.* symmetric part of the velocity gradient.

$\mathbb{I}$**:** Identity tensor.

$\mathbb{L}$**:** Renormalization matrix.

$\mathbb{T}$**:** Stress tensor.

$\mathbb{W}$**:** Spin tensor, *i.e.* anti-symmetric part of the velocity gradient.

a_{max}**:** Maximum acceleration of the tank.

c_0**:** Artificial speed of sound.

e**:** Specific internal energy.

f_0**:** Oscillation frequency of the tank.

g**:** Gravitational acceleration.

l**:** Radius of the Kernel support.

m_i**:** Mass of $i-$th particle.

m_l**:** Mass of the liquid phase.

p**:** Pressure field.

t**:** Time.

$||\mathbb{D}||$**:** Frobenius norm of tensor $\mathbb{D}$.

Re: Reynolds number.

We: Weber number.

ACKNOWLEDGEMENTS

The work was supported by the SLOWD project which received funding from the European Union's Horizon 2020 research and innovation programme under grant agreement No 815044. This work was performed by using HPC resources of the Centrale Nantes Supercomputing Centre on the cluster Liger.

The authors acknowledge Paolo Colagrossi, CEO of Punkt.ink company, for the post processing and the rendering of 3D SPH data.

DATA AVAILABILITY

The data that support the findings of this study are available from the corresponding author upon reasonable request.

DECLARATION OF INTERESTS

The authors report no conflict of interest.

REFERENCES

[1]R. Ibrahim, *Liquid sloshing dynamics: theory and applications* (Cambridge University Press, 2005).

[2]O. Faltinsen and A. Timokha, *Sloshing*, Vol. 577 (Cambridge university press Cambridge, 2009).

[3]Y. Tamura, K. Fujii, T. Ohtsuki, T. Wakahara, and R. Kohsaka, Engineering structures **17**, 609 (1995).

[4]T. Novo, H. Varum, F. Teixeira-Dias, H. Rodrigues, M. Silva, A. Costa, and L. Guerreiro, Bulletin of earthquake engineering **12**, 1007 (2014).

[5]A. Kareem, T. Kijewski, and Y. Tamura, Wind and structures **2**, 201 (1999).

[6]M. Yamamoto and T. Sone, Structural Control and Health Monitoring **21**, 634 (2014).

[7]D. Bass, Marine Technology and SNAME News **35**, 74 (1998).

[8]E. Graham and A. Rodriguez, Journal of Applied Mechanics **19**, 381 (1952).

[9]H. Abramson, NASA Special Publication **106** (1966).

[10]M. Cooker, Wave Motion **20**, 385 (1994).

[11]M. Cooker, Physics of Fluids **8**, 283 (1996).

[12]M. Perlin, W. Choi, and Z. Tian, Annual review of fluid mechanics **45**, 115 (2013).

[13]J. Frandsen, Journal of Fluids and Structures **20**, 309 (2005).

[14]H. Ardakani and T. Bridges, European Journal of Applied Mathematics **21**, 479 (2010).

[15]H. Ardakani, T. Bridges, and M. Turner, European Journal of Mechanics-B/Fluids **36**, 25 (2012).

[16]Z. Demirbilek, Ocean Engineering **10**, 347 (1983).

[17]Z. Demirbilek, Ocean Engineering **10**, 359 (1983).

[18]Z. Demirbilek, Ocean Engineering **10**, 375 (1983).

[19]D. Reed, J. Yu, H. Yeh, and S. Gardarsson, Journal of engineering mechanics **124**, 405 (1998).

[20]A. Marsh, M. Prakash, S. Semercigil, and Ö. Turan, Journal of sound and vibration **330**, 6287 (2011).

[21]B. Bouscasse, A. Colagrossi, A. Souto-Iglesias, and J. Cercos-Pita, Physics of Fluids **26**, 033103 (2014).

[22]B. Bouscasse, A. Colagrossi, A. Souto-Iglesias, and J. Cercos-Pita, Physics of Fluids **26**, 033104 (2014).

[23]F. Gambioli and A. Malan, in *International Forum on Aeroelasticity and Structural Dynamics IFASD 2017* (2017).

[24]H. Bredmose, M. Brocchini, D. Peregrine, and L. Thais, Journal of Fluid Mechanics **490**, 217 (2003).

[25]F. Gambioli and A. Malan, in *Proc. 4th Spheric Workshop, Nantes, France*, Vol. 247 (2009).

[26]B. Titurus, J. E. Cooper, F. Saltari, F. Mastroddi, and F. Gambioli, in *International Forum on Aeroelasticity and Structural Dynamics. Savannah, Georgia, USA, paper*, Vol. 139 (2019).

[27]L. Constantin, J. De Courcy, B. Titurus, T. C. Rendall, and J. Cooper, Mechanical Systems and Signal Processing **152**, 107452 (2021).

[28]L. Constantin, J. De Courcy, B. Titurus, T. Rendall, and J. Cooper, Journal of Sound and Vibration **510**, 116302 (2021).

[29]J. Martinez-Carrascal and L. González-Gutiérrez, Journal of Fluids and Structures **100**, 103172 (2021).

[30]F. Gambioli, A. Chamos, S. Jones, P. Guthrie, J. Webb, J. Levenhagen, P. Behruzi, F. Mastroddi, A. Malan, S. Longshaw, *et al.*, Proceedings of 8th Transport Research Arena TRA 2020, April 27-30, 2020, Helsinki, Finland (2020).

[31]R. Broglia and D. Durante, Computational Mechanics **62**, 421 (2018).

[32]S. Marrone, A. Colagrossi, F. Gambioli, and L. González-Gutiérrez, Phys. Rev. Fluids **6**, 114801 (2021).

[33]S. Marrone, A. Colagrossi, J. Calderon-Sanchez, and J. Martinez-Carrascal, Phys. Rev. Fluids **6**, 114802 (2021).

[34]P. Sun, A. Colagrossi, S. Marrone, M. Antuono, and A. Zhang, Computer Methods in Applied Mechanics and Engineering **348**, 912 (2019).

[35]A. Di Mascio, M. Antuono, A. Colagrossi, and S. Marrone, Physics of Fluids **29**, 035102 (2017).

[36]M. Antuono, S. Marrone, A. Di Mascio, and A. Colagrossi, Physics of Fluids **33**, 015102 (2021).

[37]E. Lamarre and W. Melville, Nature **351**, 469 (1991).

[38]S. Marrone, A. Colagrossi, A. Di Mascio, and D. Le Touzé, Physical Review E **93**, 053113 (2016).

[39]S. Gu, W. Zheng, H. Wu, C. Chen, and S. Shao, Journal of Hydraulic Research , 1 (2022).

[40]J. Calderon-Sanchez, J. Martinez-Carrascal, L. Gonzalez-Gutierrez, and A. Colagrossi, Engineering Applications of Computational Fluid Mechanics **15**, 865 (2021).

[41]S. Marrone, A. Colagrossi, A. Di Mascio, and D. Le Touzé, Journal of Fluids and Structures **54**, 802 (2015).

[42]D. Meringolo, A. Colagrossi, S. Marrone, and F. Aristodemo, Journal of Fluids and Structures **70**, 1 (2017).

[43]E. D. Christensen and R. Deigaard, Coastal engineering **42**, 53 (2001).

[44]E. D. Christensen, Coastal Engineering **53**, 463 (2006).

[45]P. Lubin and S. Glockner, Journal of Fluid Mechanics **767**, 364 (2015).

[46]E. Labourasse, D. Lacanette, A. Toutant, P. Lubin, S. Vincent, O. Lebaigue, J.-P. Caltagirone, and P. Sagaut, International journal of multiphase flow **33**, 1 (2007).

[47]D. Meringolo, S. Marrone, A. Colagrossi, and Y. Liu, Computers & Fluids **179**, 334 (2019).

[48]M. Antuono, P. Sun, S. Marrone, and A. Colagrossi, Computers & Fluids **216**, 104806 (2021).

[49]M. Antuono, A. Colagrossi, and S. Marrone, Computer Physics Communications **183**, 2570 (2012).

[50]M. Antuono, A. Colagrossi, S. Marrone, and D. Molteni, Computer Physics Communications **181**, 532 (2010).

[51]J. Smagorinsky, Monthly weather review **91**, 99 (1963).

[52]C. Bailly and G. Comte-Bellot, "The dynamics of isotropic turbulence," in *Turbulence* (Springer International Publishing, 2015) pp. 179–210.

[53]E. Y. Lo and S. Shao, Applied Ocean Research **24**, 275 (2002).

[54]B. D. Rogers and R. A. Dalrymple, in *Coastal Engineering 2004: (In 4 Volumes)* (World Scientific, 2005) pp. 415–427.

[55]J. Monaghan, Journal of Computational Physics **159**, 290 (2000).

[56]A. Khayyer, H. Gotoh, and Y. Shimizu, Journal of Computational Physics **332**, 236 (2017).

[57]J. Michel, M. Antuono, S. Marrone, and G. Oger, in *16th Int. SPHERIC workshop* (2022).

[58]A. Colagrossi, E. Rossi, S. Marrone, and D. Le Touzé, Communications in Computational Physics **20**, 660 (2016).

[59]A. Colagrossi, M. Antuono, and D. Le Touzé, Physical Review E **79** (2009).

[60]M. Antuono, S. Marrone, A. Colagrossi, and B. Bouscasse, Computer Methods in Applied Mechanics and Engineering **289**, 209 (2015).

[61]J. Cercos-Pita, M. Antuono, A. Colagrossi, and A. Souto-Iglesias, Computer Methods in Applied Mechanics and Engineering **317**, 771 (2017).

[62]S. B. Pope, *Turbulent flows* (IOP Publishing, 2001).

[63]F. Gambioli, R. A. Usach, J. Kirby, T. Wilson, and P. Behruzi, in *International Forum on Aeroelasticity and Structural Dynamics. Savannah, Georgia, USA, paper*, Vol. 139 (2019).

[64]C. Pilloton, A. Bardazzi, A. Colagrossi, and S. Marrone, European Journal of Mechanics - B/Fluids **93**, 65 (2022).

[65]P. Sagaut, *Large eddy simulation for incompressible flows: an introduction* (Springer Science & Business Media, 2006).

[66]A. Aprovitola and F. Denaro, Journal of Computational Physics **194**, 329 (2004).

[67]F. Saltari, M. Pizzoli, G. Coppotelli, F. Gambioli, J. E. Cooper, and F. Mastroddi, Journal of Fluids and Structures **109**, 103478 (2022).